Ore Geology Reviews 160 (2023) 105572

Contents lists available at ScienceDirect

Ore Geology Reviews

journal homepage: www.elsevier.com/locate/oregeorev

Petrogenesis of the Weiling beryl-bearing granitic pegmatite – A giant LCT-type pegmatite in the Northern Wuyi area, South China

Xiu-Fang Lei [a,b], Shao-Yong Jiang [a,*], Rolf L. Romer [b], Hui-Min Su [a], Ming-Yu Cao [a], Chen-Lei Zhao [c]

[a] State Key Laboratory of Geological Processes and Mineral Resources, School of Earth Resources, Collaborative Innovation Center for Exploration of Strategic Mineral Resources, China University of Geosciences, Wuhan 430074, PR China
[b] Inorganic and Isotope Geochemistry, GFZ German Research Centre for Geosciences, Telegrafenberg, 14473, Potsdam, Germany
[c] School of Earth Sciences, China University of Geosciences, Wuhan 430074, PR China

ARTICLE INFO

Keywords:
Weiling pegmatite
LCT type
Paleozoic
South China
Crustal anatexis
Beryl

ABSTRACT

The Weiling granitic pegmatite is a super-large (ca. 9.20 million tons) LCT-type pegmatite body in the Northern Wuyi area of South China, with the typical mineral assemblage quartz, plagioclase, K-feldspar and muscovite as well as tourmaline (schorl-dravite), garnet (almandine-spessartine) and beryl. This overall unzoned pegmatite with locally layered texture has economic amounts of the rare metal mineral beryl and ultrapure quartz, and porcelain clay in its uppermost weathering parts. The $^{40}Ar/^{39}Ar$ dating of pegmatitic muscovite yielded a precise age of 405.33 ± 3.38 Ma, indicating this beryl-bearing pegmatite body was formed in the Early Devonian rather than in the Jurassic-Cretaceous as previously thought. Boron and Nd isotope data demonstrate that the pegmatitic melts have solely crustal sources and are most likely derived from partial melting of the ambient metasedimentary rocks from the Zhoutan Formation. Geochemical characteristics of pegmatitic minerals muscovite, beryl, tourmaline, garnet and K-feldspar and the absence of coeval fertile granites around this pegmatite suggest that the Weiling pegmatite most likely evolved from anatectic melts that did not experience significant fractionation. The pegmatitic melts were generated by low degrees of muscovite dehydration partial melting of local metasedimentary rocks rich in fluxing elements and rare metals. These melts experienced limited differentiation during ascent in the crust. The beryl mineralization formed in the medium-temperature (222–357 °C), low-salinity (3.3–10.9 wt% NaCl equiv.) and high-density (0.62–0.86 g/cm^3) H_2O-NaCl-KCl-CO_2-N_2 system. These temperatures are much lower than typical granitic pegmatites, possibly reflecting late fluids derived from the pegmatitic magma and experienced post-crystallization alteration. The Weiling pegmatite represents a Be-bearing pegmatite that formed by partial melting of local metasedimentary rocks.

1. Introduction

Granitic pegmatites are economically important sources for metals such as Li (spodumene, petalite), Rb (lepidolite, K-feldspar), Cs (pollucite), Be (beryl), and Nb and Ta (columbite-tantalite group minerals and other Nb-Ta oxides), as well as industrial minerals such as ceramic grade feldspar, industrial mica, and ultra-pure quartz (e.g., Linnen et al., 2012 and references therein). Granitic pegmatites are divided into five classes: abyssal, muscovite, muscovite-rare-element, rare-element and miarolitic from deep- to low-seated environment of formation. Furthermore, rare-metal pegmatites are also commonly classified as LCT (Li, Cs, Ta), NYF (Nb, Y, F), and LCT-NYF mixed types (Cerny and Ercit, 2005).

Granitic pegmatites traditionally have been interpreted to be the extreme result of extended fractional crystallization of a granitic magma and are often located around huge granitic batholiths and stocks (Černý 1991; London 2005). Pegmatites at different distances from the intrusion could differ with respect to element association and mineral assemblage (Cerny and Ercit, 2005). Such an interpretation implies a close spatial and temporal relation between granitic intrusions and pegmatites. Parental granites would have to be several orders of magnitude larger than the pegmatites (Partington et al., 1995). Fractionated pegmatites are usually distributed within a radius of 10–15 km centered on the parent granite (Jiang et al., 2021). But not all rare-metal pegmatites are associated with granitic intrusions, and such pegmatites

* Corresponding author.
E-mail address: shyjiang@cug.edu.cn (S.-Y. Jiang).

https://doi.org/10.1016/j.oregeorev.2023.105572
Received 31 January 2023; Received in revised form 23 June 2023; Accepted 21 July 2023
Available online 23 July 2023

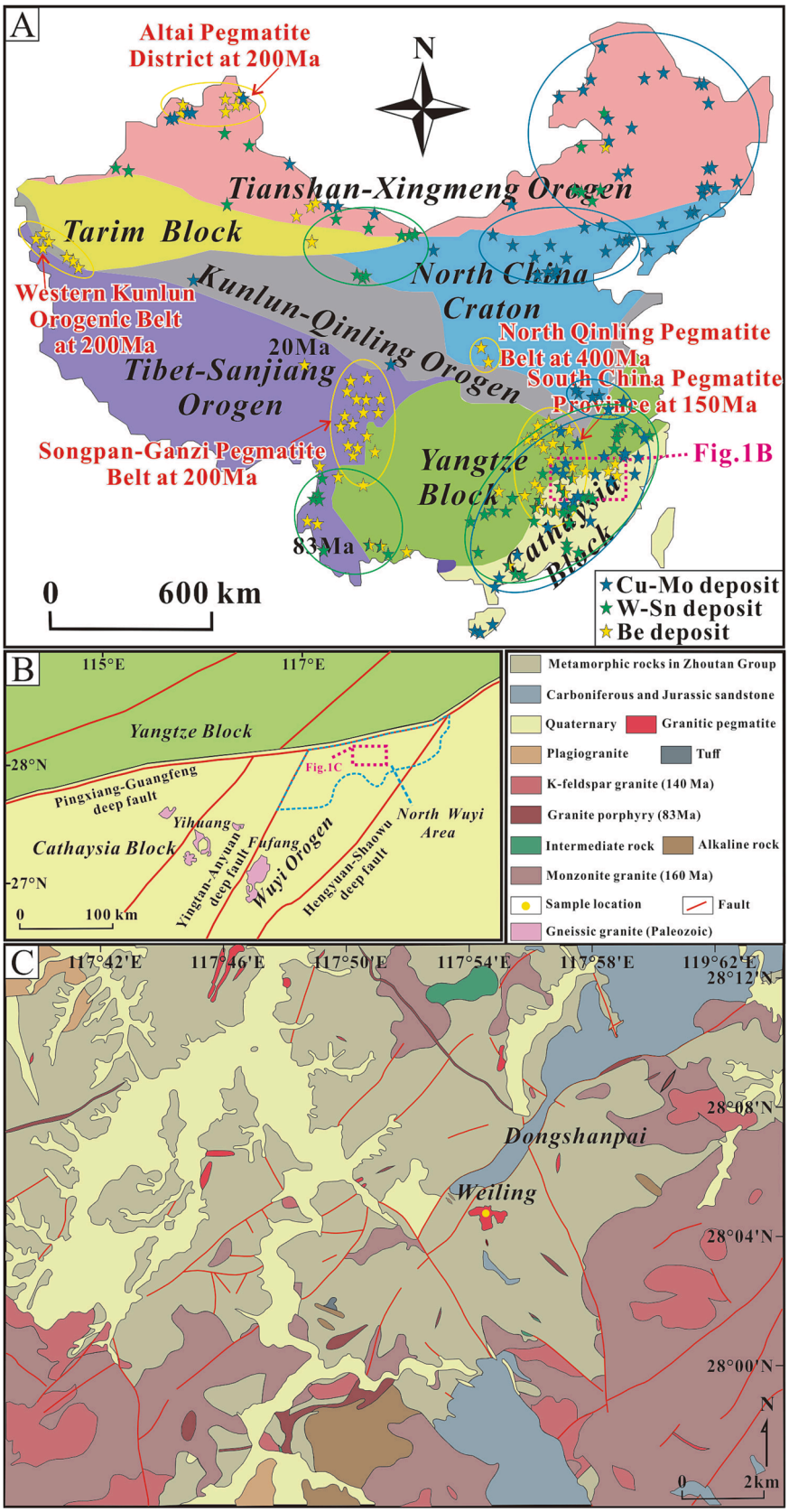

Fig. 1. (A) Tectonic map of China showing the distribution of Be deposits (Dai et al., 2014; Li et al., 2017; Yan et al., 2022), W-Sn deposits (Mao et al., 2019), and Cu-Mo deposits (Zeng et al., 2013; Zhong et al., 2017); (B) Regional geological map of the North Wuyi area (modified from Dai et al., 2014); (C) Geological sketch map of the Weiling granitic pegmatite (modified from BGMEDJP 2017).

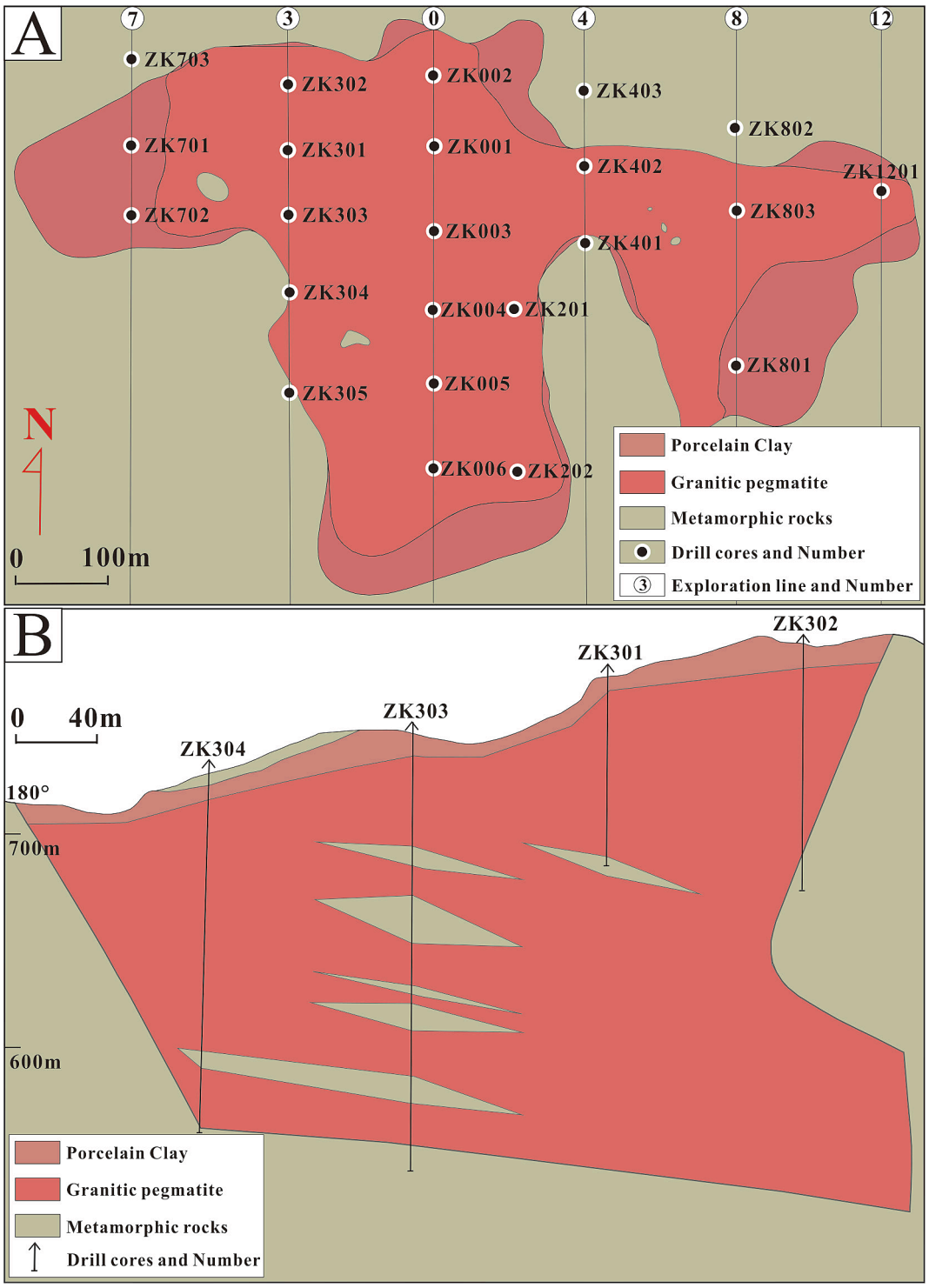

Fig. 2. (A) Simplified geological map and (B) profile (exploration line 3) of the Weiling pegmatite (modified from BGMEDJP 2017).

are interpreted to have formed directly by low-degree partial melting of crustal lithologies rich in fluxing elements and rare metals, which have experienced only limited differentiation during ascent in the crust (Martin and De Vito, 2005; Müller et al., 2012; Zhao et al., 2015). The spatial distribution of these pegmatites is controlled by the distribution of fertile source rocks and P-T conditions that allow for partial melting. The age of these pegmatites corresponds to the age of regional metamorphism or post-metamorphic crustal extension (Müller et al., 2017). The wall rocks of such pegmatites include schist, gneiss, migmatite, granite, and gabbro. These wall rocks control which rare metals become particularly enriched in anatectic pegmatites (Liu et al., 2020).

In China, there exist four large rare-metal pegmatite districts (Fig. 1A), including the Altai Pegmatite District, the Western Kunlun Orogenic Belt (e.g., the Bailongshan pegmatite), the Songpan-Ganzi Pegmatite Belt (e.g., the Jiajika pegmatite), and the South China Pegmatite Province (e.g., the Nanping pegmatite and Mufushan pegmatite) (Yan et al., 2022). In addition, there are several small districts with rare-metal pegmatites such as the North Qinling Pegmatite Belt (Li et al., 2014). Locally, beryl-bearing deposits occur in these pegmatite districts of China (Li et al., 2017). In the South China Block,

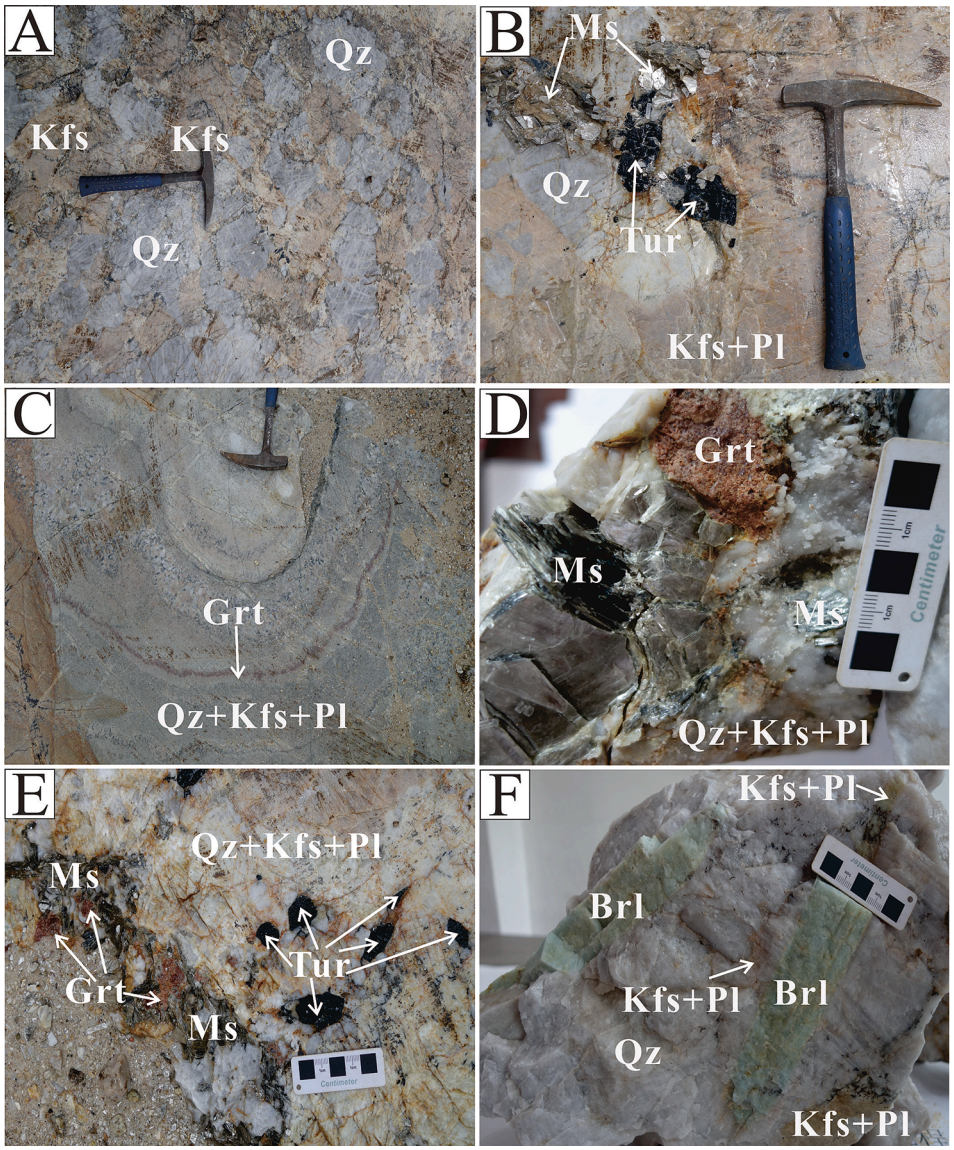

Fig. 3. (A) Graphic texture formed by K-feldspar and quartz; (B) Pegmatite with typical mineral association of tourmaline-muscovite-quartz-K-feldspar-plagioclase; (C) Distribution of garnet in the layered structure; (D) Coarse-grained garnet coexisting with large flake muscovite in the pegmatite; (E) Pegmatite with typical mineral association of garnet-tourmaline-muscovite-quartz-K-feldspar-plagioclase; (F) Beryl crystals in the pegmatite. Abbreviations: Ms = Muscovite; Qz = Quartz; Tur = Tourmaline; Kfs = K-feldspar; Pl = Plagioclase; Grt = Garnet; Brl = Beryl.

Be-pegmatites are rare and most Be resources are bound to minerals in hydrothermal quartz-vein W-Sn-Be deposits related to granitic intrusions (Li et al., 2017; Fig. 1A).

The recently-discovered Weiling pegmatite in the South China Block is a super-large granitic pegmatite body that contains significant amounts of beryl and ultra-pure quartz (Zheng et al., 2023). This pegmatite was originally mined for porcelain clay and recently was mined for industrial mineral feldspar and quartz. During mining, coarse-grained green beryl crystals were found. The proven reserves of 9.20 million tons of granitic pegmatite are of superior quality and account for the high economic value of the Weiling granitic pegmatite. Except for the huge quantity of feldspar and quartz, coarse-grained beryl within the Weiling pegmatite can be mined as rare metal source. Until now, little is known about the Weiling pegmatite that could be helpful for guiding exploration for similar pegmatites and Be resources. As the spatial distribution and the formation conditions of pegmatites that are the product of extreme fractional crystallization and of low-volume partial melting differ and have contrasting optimal approaches for regional prospecting, a better understanding for the formation of the Weiling pegmatite is essential. In particular information on the age, tectonic setting, petrogenesis, and source rocks is relevant, as this information could provide guidelines for exploration on the regional scale for other rare-metal pegmatites. In this paper, we present the results of muscovite Ar-Ar dating and garnet U-Pb dating, and use the major and trace element compositions of muscovite, beryl, tourmaline, garnet, and K-feldspar, in combination with B (tourmaline) and Nd (garnet, and feldspar) isotope data and fluid inclusions data to constrain the petrogenesis of the Weiling pegmatite.

2. Geological setting

2.1. Tectonic development and granitic magmatism of the South China Block

The South China Block (SCB), well known for its large-scale Mesozoic granitic magmatism and related Sn and W mineralization, includes two major Precambrian continental blocks, namely the Yangtze Block in the northwest and the Cathaysia Block in the southeast (Fig. 1A). The Yangtze Block is composed mainly of late Paleoproterozoic and Neoproterozoic rocks and local Archean rocks, whereas the Cathaysia Block is dominated by metamorphosed Paleoproterozoic volcano-sedimentary units (Shu et al., 2008). The SCB formed by amalgamation of the Yangtze and Cathaysia blocks at ca. 830 Ma along the Jiangshan-Shaoxing-Pingxiang-Guanxian suture (Fig. 1B). A second collision between the

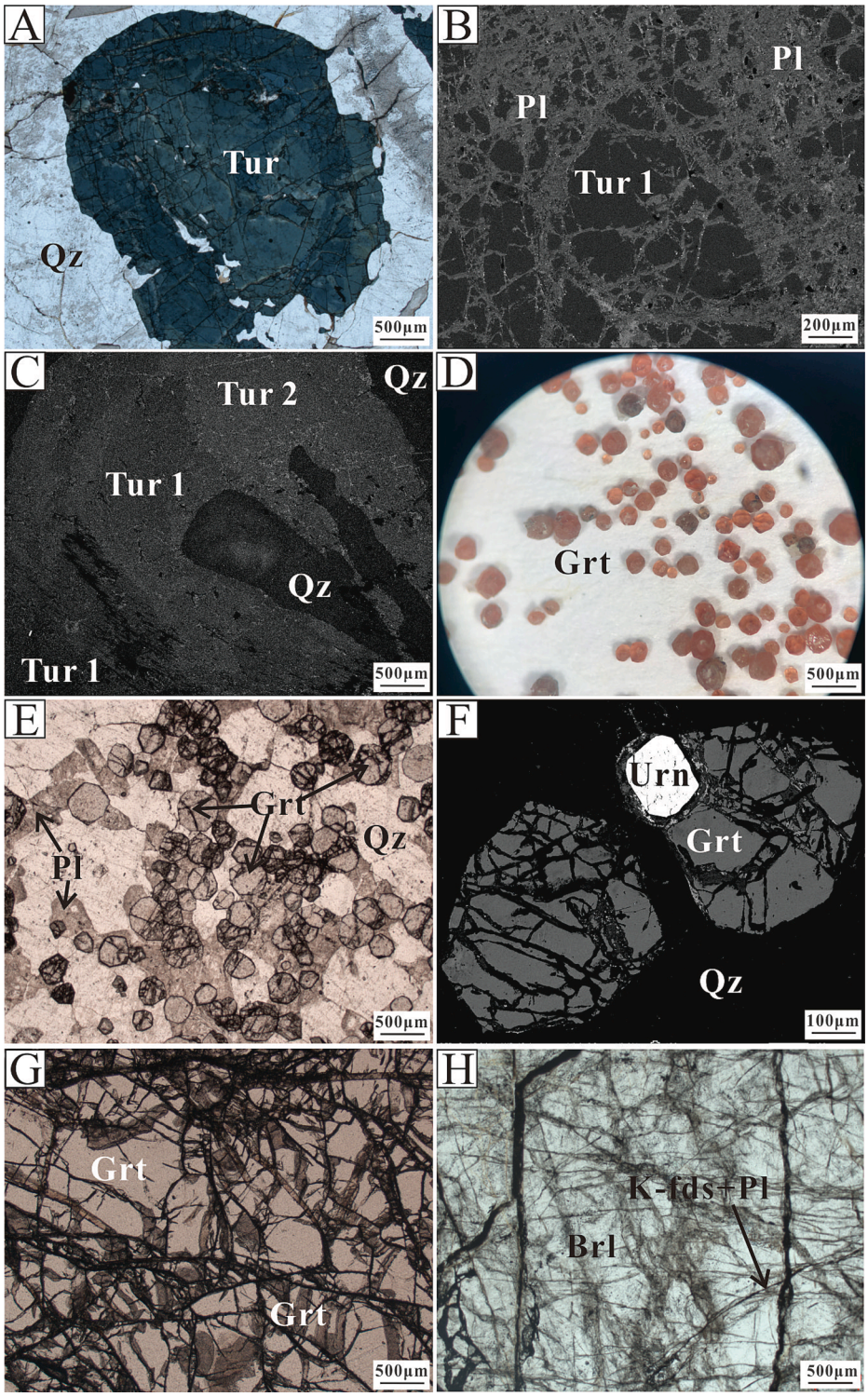

Fig. 4. Microphotograph of the Weiling pegmatite samples. (A) Tourmaline crystal with weak zonation under the polarized light microscope; (B) Homogenous tourmaline grains cut by plagioclase veinlets; (C) Compositional zoning of tourmaline in BSE images; (D) The small-grained garnet showing different colors (mostly pink) under the ordinary light; (E) The small-grained garnet occurring in layers under the polarized light microscope; (F) Homogenous garnet grains in layers in BSE images; (G) Homogenous garnet grains in coarse-grained pegmatite in BSE images; (H) Metasomatic beryl under the polarized light microscope. Abbreviations: Qz = Quartz; Tur = Tourmaline; Grt = Garnet; Brl = Beryl; Pl = Plagioclase; Urn = Uraninite. (For interpretation of the references to color in this figure legend, the reader is referred to the web version of this article.)

Yangtze and Cathaysia blocks in the Early Paleozoic (ca. 420–440 Ma) caused intense deformation and plutonism (Wang et al., 2007a). There was major reactivation of old structures within these blocks during subsequent tectonic events at the margins of the SCB, such as the Silurian closure of the Paleo-Tethys (collision along the Qinling Belt), the Triassic closure of the Meso-Tethys during the collision of Sibumasu, the Jurassic and Cretaceous subduction of the Paleo-Pacific, and the Cenozoic closure of the Neo-Tethys (Shu et al., 2008; Wang et al., 2011).

There are multiple stages of granitic magmatism associated with these tectonic events, whereby the nature of the rocks and their potential to form mineralization differs with time and regional occurrence. Early Paleozoic syn- to post-orogenic granites are dominated by biotite granites, two-mica granites, and granodiorites that mainly occur in the Jiangnan, Wuyi, Nanling, and Yunkai domains (Song et al., 2015). Most of these granitoids are peraluminous S-type granitoids that are derived from anatexis of the continental crust. Only few Early Paleozoic granitoids have I-type compositions (Li et al., 2011b). Early Paleozoic rare metal pegmatites are rare in the SCB. Examples include the Nanping Ta-Nb-Sn pegmatite (387 Ma, Tang et al., 2017) and the Xigang Nb-Ta-Li pegmatite (420 Ma, Che et al., 2019). In contrast, Jurassic to

Cretaceous (Yanshanian) (160–80 Ma) granites in the SCB are voluminous and carry important Sn-greisen and W-vein type deposits and locally Be mineralization (Chen et al., 2013; Hua et al., 2013).

2.2. The Weiling pegmatite in the Northern Wuyi area

The basement of the Northern Wuyi area (NWA), which is located in the northeastern part of the Cathaysia Block (Fig. 1B), mainly consists of Mesoproterozoic and Early Cambrian metamorphic rocks, i.e., muscovite-quartz schist, biotite schist, biotite-plagioclase granulite, plagioclase amphibolite, and marble. The metamorphic basement is uncomfortably overlain by Devonian and Carboniferous to Cenozoic sedimentary rocks of limestone, chert, sandstone, and siltstone (Fig. 1C). The structure of the NWA is dominated by three deep fault systems (Fig. 1B), i.e., the EW-striking Pingxiang-Guangfeng fault at its northern boundary, which also represents the suture between the Yangtze and Cathaysia blocks, the NNE-striking Yingtan-Anyuan fault at its western boundary, and the NE-striking Heyuan-Shaowu fault, which plays a key role in the distribution of Jurassic to Cretaceous magmatic rocks and associated polymetallic mineralization. Minor faults are predominantly NE-SW trending (Fig. 1C). Intrusive rocks are widely distributed in the NWA (Fig. 1C), and most of them formed during the Late Jurassic and Late Cretaceous. Around the Weiling pegmatite in the NWA, there occur additional pegmatites, e.g., Dongshanpai pegmatite, whose age and petrogenesis are not known either until now (Fig. 1C; Zheng et al., 2023). Although there exist Early Paleozoic granites, e.g., Yihuang and Fufang gneissic granites, adjacent to the southwest of the NWA, they are relatively small and far away (≫ 10–15 km) from the Weiling pegmatite (Fig. 1B). No related parental granite pluton has been found so far. The Weiling super-large granitic pegmatite body, located in the NWA (Fig. 1C and 2), is hosted by Neoproterozoic marine sedimentary sequences intercalated with mafic volcanic rocks of the Zhoutan Formation. These rocks were metamorphosed in the Late Neoproterozoic and migmatized in the Early Paleozoic (446–423 Ma; Zhao et al., 2021; BGMEDJP, 2017). The basement rocks are unconformably overlain by post-Devonian sedimentary rocks and intruded by Jurassic to Cretaceous granites (Li et al., 2011a). The Weiling pegmatite body is exposed in a 1100 m long and 200–500 m wide area (Fig. 2A). Limited drill core data reveal a depth of 50–250 m (Fig. 2B). The top of the granitic pegmatite has been weathered into sandy kaolin (porcelain clay), with a thickness of 5–10 m (locally > 50 m) (Fig. 2B). There is a gradual transition from porcelain clay to fresh granitic pegmatite.

The Weiling pegmatite shows no association with the regional NE-SW trending faults (Fig. 1C), and does not show internal zonation from the boundary to the central parts. The pegmatite is heterogenous, both with respect to grain size and distribution of the minerals tourmaline, garnet, and beryl. Locally, there exists complex banding with variations in thickness and fineness. The Weiling granitic pegmatite is typically composed of plagioclase (40 vol%), K-feldspar (20 vol%), quartz (20 vol%), muscovite (5–10 vol%) and minor tourmaline (7 vol %), garnet (5 vol%), and beryl (3 vol%). K-feldspar and quartz are intergrown and show graphic texture (Fig. 3A). Tourmaline displays radial to dendritic morphology with both needle-like, long columnar and massive tourmaline aggregates (Fig. 3B, E). Tourmaline crystals are generally polychromatic, and some crystals display optical zonation, with greenish to yellowish cores and dark-green rims under plane polarized light (Fig. 4A). Two groups of tourmaline are distinguished in BSE images, e.g., Tur 1 which is homogenous and cut off by plagioclase veinlets (Fig. 4B, C), and Tur 2 which occurs as the irregular alteration zoning of Tur 1 (Fig. 4C). There are two types of garnet, among which one is fine-grained (20–200 μm), which forms idiomorphic crystals that are red, brown, black, and gray and form layers (Fig. 3C, 4D, E). It should be noted that variable colors for tourmaline and garnet under natural light and the optical microscope do not correspond to compositional changes in BSE images (Fig. 4A-F). Alternating bands rich in fine-grained garnet and in K-feldspar, plagioclase, and quartz form concentric structures on the decimeter scale within the pegmatite (Fig. 3C). Another type of garnet forms 2–3 cm large brown crystals (Fig. 3D, E, 4G) that occur together with coarse-grained muscovite, tourmaline, K-feldspar, plagioclase, and quartz. Light green prismatic beryl occurs together with coarse-grained quartz and feldspar (Fig. 3F). Beryl crystals are fractured and the fractures are filled with fine-grained K-feldspar and plagioclase veinlets (Fig. 4H).

Samples for analysis were collected from different depths of the 95-m drill hole ZK301 and the surface outcrop. From top to bottom of drill hole ZK301, the lithology varies from coarse-grained K-feldspar-quartz pegmatite with graphic texture, coarse-grained tourmaline-muscovite-K-feldspar-quartz pegmatite, interbedded layered domains (layers are 0.5–1 cm wide in the depth range 64.0–68.5 m), to coarse-grained tourmaline-muscovite-K-feldspar-quartz pegmatite with minor garnet and beryl. Based on grain size and color, five domains are distinguished in the layered structure from the center to the rim, i.e., bright fine-grained layer, gray fine-grained layer, gray fine-medium layer, and garnet-bearing layer, and medium-coarse size domains. These layer domains represent a small-scale, irregular local structures (Fig. 3C). Bright fine-grained layers consist only of K-feldspar and quartz. The color change in the fine-grained layer from white to gray is due to the presence of tourmaline. The local structures are not representative for the whole pegmatite. In particular, they are not comparable to the complex zoning typical for pegmatites related to highly fractionated leucogranite with zoning variations of lithology. Muscovite used for Ar-Ar dating was sampled from a coarse-grained section of the tourmaline-muscovite-feldspar-quartz pegmatite. Muscovite occurs as flaky euhedral crystals or 2–5 cm large fine-grained nearly monomineralic aggregates (Fig. 3D). Muscovite from these boundaries shows only a little alteration along grain boundaries (Fig. 3D).

3. Analytical methods

3.1. $^{40}Ar/^{39}Ar$ dating of muscovite

Muscovite was separated from a coarse-grained muscovite-quartz-feldspar pegmatite sample to determine the age of Weiling granitic pegmatite using the $^{40}Ar/^{39}Ar$ method. Muscovite with 99% purity was separated from the 60–80 mesh fraction. Muscovite separates were irradiated at the atomic reactor at the Research Institute of Atomic Energy (Beijing, China). Biotite ZHB-25 from the Beijing Fangshan granodiorite (132.7 ± 1.2 Ma; Wang 1983) was used as a monitor standard. The J factor was 0.42901%, the neutron flux was about 2.60×10^{13}n cm^{-2} s^{-1}, and the integrated neutron flux was 2.25×10^{18}n cm^{-2}. Step-heating $^{40}Ar/^{39}Ar$ analyses were performed at the Beijing Research Institute of Uranium Geology following the protocol given by Chen et al. (2006). Measured isotopic ratios were corrected for mass discrimination, atmospheric Ar contributions, blanks, and irradiation-induced mass interferences. Correction factors for interfering argon isotopes derived from Ca and K are: $(^{39}Ar/^{37}Ar)_{Ca} = 0.000806$, $(^{36}Ar/^{37}Ar)_{Ca} = 0.0002389$, and $(^{40}Ar/^{39}Ar)_{K} = 0.004782$. All dates are reported using 5.543×10^{-10} a^{-1} as the total decay constant for ^{40}K (Steiger and Jäger, 1977). The errors are 2σ deviations and correspond to the 95% confidence level. The Ar-Ar age data were calculated and plotted using the *ArArCALC v. 2.4* (Koppers 2002).

3.2. U-Pb dating of garnet

Garnet U-Pb isotopic dating was carried out at GFZ German Research Center for Geosciences (Potsdam). Isomorphic fine-grained garnet was separated from two pegmatite samples (15WL-14 and 15WL-16) from a local structure with concentric garnet-rich layers (Fig. 3C). For garnet U-Pb dating, only red translucent garnet grains without visible inclusions were separated under the binocular microscope. Black and grey garnet, as well as garnet with visible intergrowths were removed. Before analysis, garnet was washed in turn using warm 7 N HNO_3, H_2O, and

Table 1
$^{40}Ar/^{39}Ar$ step-heating geochronology data for muscovite from the Weiling granitic pegmatite.

T (°C) [a]	$(^{40}Ar/^{39}Ar)_m$ [b]	$(^{36}Ar/^{39}Ar)_m$ [b]	$(^{37}Ar/^{39}Ar)_m$ [b]	$^{40}Ar^*$ (%) [c]	F ($^{40}Ar^*/^{39}Ar$) [d]	^{39}Ar ($\times10^{-14}$mol)	^{39}Ar (%)	Age (Ma) [e]	±2σ (Ma)
700	42.8190	0.0531	5.52E-05	63.27	27.09	0.04	0.05	200.2	7.2
800	30.3341	0.0162	1.10E-05	84.17	25.53	0.26	0.32	189.3	2.4
850	36.2419	0.0225	6.74E-06	81.56	29.56	0.42	0.51	217.4	2.8
900	36.4318	0.0089	2.88E-06	92.73	33.78	1.10	1.35	246.4	2.4
950	58.4000	0.0004	9.12E-07	99.75	58.25	31.10	38.22	406.2	3.8
1000	58.3020	0.0005	9.60E-07	99.73	58.14	30.10	36.99	405.5	3.6
1050	58.2278	0.0008	1.90E-06	99.56	57.97	2.55	3.13	404.4	3.6
1100	64.1744	0.0008	2.10E-06	99.59	63.91	2.77	3.40	441.2	4.0
1150	63.4529	0.0004	1.06E-06	99.78	63.31	11.47	14.10	437.5	4.0
1200	61.5539	0.0027	1.91E-06	98.68	60.74	1.40	1.73	421.7	3.8
1300	71.1526	0.0311	1.89E-05	87.05	61.94	0.16	0.20	429.1	4.6

[a] Temperature of each step-heating, time of each step-heating is 10 min.
[b] Measured isotopic ratios.
[c] Radiogenic Ar.
[d] Calculated isotopic ratio of radiogenic Ar to ^{39}Ar produced by neutron interactions on ^{39}K be obtained.
[e] Age spectrum of muscovite during step-heating.

acetone. A mixed ^{205}Pb-^{235}U tracer was added and dried before sample dissolution in 40% HF on a hotplate (160 °C) for 5 days. Lead and U were separated using Biorad AG-1 and a two-stage HBr-HCl-HNO_3 ion exchange column chemistry (Romer et al., 2005). Lead and U were loaded with dilute H_3PO_4 and silica gel on separate Re single-filaments and their isotopic compositions were determined using a Thermo-Fisher-Scientific Triton multi-collector thermal ionization mass-spectrometer operated in static multicollection mode, using Faraday collectors and an ion counter. Lead and U were analyzed at 1160–1260 °C and 1300–1360 °C, respectively.

3.3. Major and trace element analysis of pegmatitic minerals

Major and trace element compositions of various minerals (muscovite, beryl, tourmaline, garnet, and K-feldspar) from the pegmatite were determined at the State Key Laboratory of Geological Processes and Mineral Resources (GPMR) at China University of Geosciences (Wuhan). Major elements were analyzed using a JEOL JXA-8100 Electron Probe Micro Analyzer operated at 15 kV acceleration voltage and 20nA beam current. Data were corrected on-line using a modified ZAF correction procedure. The peak counting time was 10 s for Na, Mg, Al, Si, K, Ca, Fe and 20 s for Ti, Mn, F and Cl. The following standards were used: sanidine for K, pyrope garnet for Fe and Al, diopside for Ca and Mg, jadeite for Na, rhodonite for Mn, olivine for Si, rutile for Ti, topaz for F and halite for Cl. *In-situ* trace element analyses were obtained on polished thin sections using a RESOlution S-155 laser ablation system coupled to a Thermo iCAP Qc inductively coupled plasma mass spectrometry (LA-ICP-MS). NIST SRM 612 and 610 glass standards and USGS reference glasses BIR-1G, BCR-2G and BHVO-2G were used for external calibration and were repeatedly analyzed after each 7–10 samples to correct for signal drift. Standards and samples were ablated using a 33 μm beam diameter, 10 Hz repetition rate, and a fluence of ~ 3 J/cm^2. The isotope ^{29}Si was used as the internal standard in conjunction with the Si concentrations determined by electron microprobe. Reduction of raw data was performed offline using the ICP-MS-Data-Cal software (Liu et al., 2010).

3.4. Boron isotope analysis

The boron isotopic composition of tourmaline samples was determined by using RESOlution S-155 laser ablation system coupled to a Nu plasma II multi-collector ICPMS (LA-MC-ICP-MS) at the GPMR, China University of Geosciences (Wuhan). Analyses were carried out using 50 μm beam diameter, 10 Hz repetition rate, and 3 J/cm^2 fluence. Counting time were 30 s for the background and 40 s for the sample. The ^{11}B and ^{10}B signals were collected using static multi-collection and Faraday cups. Instrumental mass fractionation was corrected using the standard–sample–standard bracketing method and the international tourmaline standard IAEA B4 ($\delta^{11}B = -8.71$ ‰, Tonarini et al., 2003) as external standard. Instrumental mass fractionation (IMF) and analytical quality were assessed by replicate analyses of tourmaline reference materials dravite (HS#108796) and schorl (HS#112566) from the Harvard Mineralogical Museum (Dyar et al., 2001).

3.5. Neodymium isotope analysis

The Nd isotopic compositions of garnet and feldspar were determined using a TRITON multi-collector thermal ionization mass spectrometer at GFZ German Research Center for Geosciences (Potsdam). Before dissolution, mineral concentrates were cleaned using 7 N HNO_3 and a mixed ^{149}Sm-^{150}Nd tracer was added. Samples were dissolved in teflon beakers on the hotplate using 40% HF. Rubidium and Sr were separated in 2.5 N HCl medium by using cation-exchange techniques (Bio Rad AG50 W-X8). After Rb and Sr were collected, Ba was washed out using 2.5 N HNO_3 before REEs were eluted using 6 N HCl. Neodymium and Sm were separated from the other REEs by cation-exchange chromatography using HDEHP-coated Teflon in 0.22 N and 0.4 N HCl medium, respectively. Strontium and Rb were loaded on separate single Ta -filaments and analyzed using dynamic multi-collection. Neodymium and Sm were loaded on separate double Re -filaments and analyzed using dynamic multi-collection.

3.6. Fluid inclusion measurements

Fluid inclusions in quartz and beryl were analyzed using doubly polished thin sections. Typical fluid inclusion assemblages (FIA), i.e., groups of temporally coeval inclusions occurring in clusters and trails or along individual growth zones (Goldstein and Reynolds, 1994) were selected for micro-thermometric measurements and laser Raman spectroscopic analysis. The petrographic study of fluid inclusion was conducted used a Nikon Eclipse LV100POL microscope at the National Demonstration Center for Experimental Mineral Exploration Education, China University of Geosciences (Wuhan). Micro-thermometric measurements were carried out by using a Linkam THMS-600 heating-freezing stage (from −196 to 600 ℃) and liquid N_2 as a cooling agent. The stage was calibrated using fluid inclusions of pure H_2O (ice melting temperature = 0 ℃, critical temperature = 371.4 ℃) and pure CO_2 (CO_2 melting temperature = -56.6 ℃). The estimated precision of temperature is ± 0.5 ℃ for temperature between −120 and −70 ℃, ± 0.2 ℃ for temperature in the range of −70 to 100 ℃, and ± 2 ℃ for temperature higher than 100 ℃. Heating and freezing rates near the point of phase transformation are 1–10 ℃/min and 0.1–1 ℃/min, respectively. Ice melting temperatures were determined at a heating rate of 0.1 ℃/min, and homogenization temperatures at a rate of 1 ℃/min. Freezing

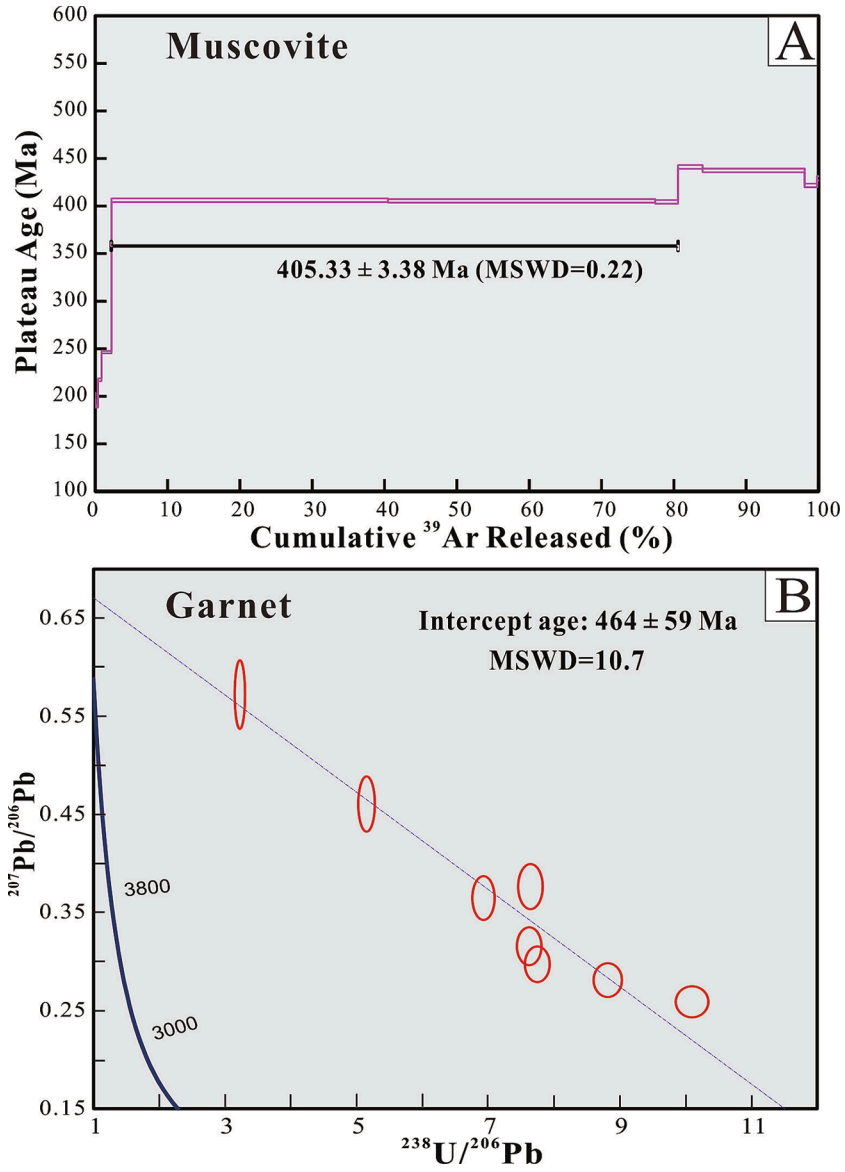

Fig. 5. Age of pegmatite minerals from the Weiling granitic pegmatite. (A) ^{40}Ar/^{39}Ar step-heating geochronological data for muscovite. The plateau age is defined by three fractions accounting for 80% of the radiogenic Ar. (B) Tera-Wasserburg diagram for garnet U-Pb dating. Data from Tables 1 and 2.

Table 2
U-Pb geochronology data for garnet from the Weiling granitic pegmatite.

Sample Name	U (ppm) [a]	Pb (ppm) [a]	^{238}U/^{204}Pb [b]	^{206}Pb/^{204}Pb [b]	^{207}Pb/^{204}Pb [b]	^{208}Pb/^{204}Pb [b]	^{238}U/^{206}Pb [c]	2 σ	^{207}Pb/^{206}Pb [c]	2 σ
15WL-14	1.03	0.20	558	63.28	17.79	43.84	8.82	0.18	0.281	0.014
15WL-14	0.30	0.24	90	27.78	15.89	38.05	3.22	0.06	0.572	0.029
15WL-14	0.53	0.14	349	45.65	17.19	39.37	7.64	0.15	0.376	0.019
15WL-14	0.50	0.21	183	35.62	16.41	38.50	5.15	0.10	0.461	0.023
15WL-16	3.60	0.56	702	69.81	17.99	38.65	10.05	0.20	0.258	0.013
15WL-16	1.86	0.43	419	55.03	17.37	38.96	7.62	0.15	0.316	0.016
15WL-16	2.35	0.65	321	46.35	16.91	38.79	6.93	0.14	0.365	0.018
15WL-16	2.41	0.53	459	59.21	17.59	38.82	7.74	0.15	0.297	0.015

[a] Concentrations of Pb and U were determined by isotope dilution using a mixed ^{205}Pb-^{235}U tracer.
[b] Measured isotope ratios corrected for fractionation and isotopic tracer.
[c] Corrected for fractionation, 15 pg Pb blank, 1 pg U blank, isotopic tracer and initial lead.

temperatures were measured before heating temperatures. Salinities for aqueous fluid inclusions were calculated using the final ice melting temperature (Bodnar and Vityk, 1994). For CO_2-bearing fluid inclusions, salinities were calculated by using the melting temperature of clathrate (Darling 1991). Qualitative determinations of the compositions of individual fluid inclusion were conducted by using an RM-1000 laser Raman probe at GPMR, China University of Geosciences (Wuhan). The Ar^+ laser has 514.5 nm wavelength and 5 mW power. Measurements were performed at 2 cm^{-1} resolution, 20–40 s exposure, and for the range 50 to 3500 cm^{-1}. The spectrograph aperture was confined to 50

Table 3
Chemical compositions of muscovite in the Weiling pegmatite.

Major elements (wt%)										
Na2O	0.48	0.60	0.25	0.26	0.17	0.43	0.47	0.47	0.53	0.58
MgO	0.72	0.72	0.68	0.68	0.74	0.64	0.65	0.68	0.65	0.74
Al2O3	33.72	34.45	33.37	33.68	34.06	33.53	33.94	33.72	33.60	33.88
SiO2	46.57	47.63	46.57	46.99	47.54	47.87	47.54	47.46	46.95	47.77
FeO	2.92	2.46	2.88	2.80	2.88	3.56	3.14	3.31	3.36	3.17
MnO	0.02	0.05	0.03	0.05	0.03	0.03	0.01	0.00	0.07	0.05
TiO2	0.11	0.09	0.18	0.07	0.09	0.06	0.10	0.12	0.08	0.14
CaO	0.08	0.05	0.04	0.06	0.05	0.02	0.02	0.09	0.06	0.06
K2O	9.39	9.11	9.32	8.41	7.49	10.11	10.19	9.96	10.07	10.06
F	0.14	0.16	0.07	0.15	0.05	0.00	0.01	0.01	0.02	0.03
Cl	0.01	0.01	0.00	0.01	0.01	0.00	0.02	0.00	0.01	0.00
Total	94.13	95.31	93.38	93.14	93.10	96.29	96.09	95.97	95.38	96.46
Si	3.14	3.15	3.16	3.17	3.19	3.17	3.15	3.16	3.14	3.16
Al^{IV}	0.86	0.85	0.84	0.83	0.81	0.83	0.85	0.84	0.86	0.84
Al^{VI}	1.82	1.84	1.83	1.85	1.88	1.79	1.81	1.80	1.80	1.79
Ti	0.01	0.00	0.01	0.00	0.00	0.00	0.00	0.01	0.00	0.01
Fe^{3+}	0.16	0.14	0.16	0.16	0.16	0.20	0.17	0.18	0.19	0.17
Mn	0.00	0.00	0.00	0.00	0.00	0.00	0.00	0.00	0.00	0.00
Mg	0.07	0.07	0.07	0.07	0.07	0.06	0.06	0.07	0.06	0.07
Ca	0.01	0.00	0.00	0.00	0.00	0.00	0.00	0.01	0.00	0.00
Na	0.06	0.08	0.03	0.03	0.02	0.06	0.06	0.06	0.07	0.07
K	0.81	0.77	0.81	0.72	0.64	0.85	0.86	0.84	0.86	0.85
Total	6.94	6.90	6.91	6.85	6.79	6.97	6.97	6.97	6.99	6.98
MF	0.30	0.34	0.29	0.30	0.31	0.24	0.27	0.27	0.25	0.29
$Al^{VI}+Fe^{3+}+Ti$	1.99	1.98	2.00	2.01	2.05	1.99	1.99	1.99	1.99	1.97
Fe^{2+}+Mn	0.00	0.00	0.00	0.00	0.00	0.00	0.00	0.00	0.00	0.00
Ti/(Mg + Fe + Ti + Mn)	0.02	0.02	0.04	0.02	0.02	0.01	0.02	0.02	0.02	0.03
Al/(Al + Mg + Fe + Ti + Mn + Si)	0.44	0.44	0.44	0.44	0.44	0.43	0.44	0.44	0.44	0.44
Trace elements and rare earth elements (ppm)										
Sn	57.6	54.4	51.3	54.1	54.5	57.6	67.0	58.1	58.0	51.1
Nb	149	142	139	152	144	143	319	141	219	179
Ta	8.63	8.36	8.45	8.86	8.75	9.21	30.5	9.81	27.1	25.8
Li	27.0	24.1	22.4	30.0	21.9	20.6	30.1	33.8	30.9	23.4
Sc	19.5	19.4	19.4	19.4	19.2	20.6	15.4	16.7	14.5	15.5
Zn	68.7	67.4	67.3	81.3	77.4	72.9	87.6	85.7	83.8	83.3
Ga	107	106	105	103	104	105	102	100	100	101
Ge	2.01	1.49	1.92	1.66	1.68	2.32	1.89	1.99	1.67	1.71
V	0.11	0.16	0.15	0.11	0.41	0.10	0.70	0.42	0.94	0.75
Cr	0.49	0.55	0.37	0.55	0.48	0.01	0.04	0.31	0.28	0.29
Co	0.33	0.46	0.57	0.23	0.34	0.13	0.43	0.28	0.24	0.41
Ni	0.00	0.16	0.00	0.37	0.00	0.13	0.36	0.00	0.07	0.18
Cu	1.09	0.60	1.01	0.98	0.40	1.33	1.87	0.42	0.72	3.30
Mo	0.09	0.08	0.06	0.09	0.12	0.06	0.07	0.05	0.05	0.08
Cd	0.05	0.03	0.01	0.02	0.00	0.00	0.01	0.01	0.02	0.00
In	0.21	0.20	0.21	0.23	0.24	0.26	0.23	0.19	0.20	0.26
Sb	0.02	0.00	0.06	0.02	0.00	0.00	0.01	0.02	0.02	0.02
La	0.00	0.00	0.01	0.00	0.00	0.01	0.00	0.00	0.00	0.01
Ce	0.00	0.00	0.02	0.00	0.00	0.02	0.01	0.00	0.00	0.01
Pr	0.00	0.00	0.00	0.00	0.00	0.00	0.00	0.00	0.00	0.00
Nd	0.01	0.00	0.00	0.00	0.02	0.02	0.01	0.00	0.00	0.00
Sm	0.02	0.01	0.00	0.00	0.00	0.00	0.00	0.00	0.00	0.00
Eu	0.04	0.00	0.01	0.00	0.03	0.01	0.00	0.00	0.00	0.00
Gd	0.30	0.81	0.00	0.18	0.00	0.00	0.13	0.65	0.00	0.12
Tb	0.01	0.00	0.00	0.00	0.00	0.00	0.00	0.00	0.00	0.00
Dy	0.00	0.00	0.01	0.00	0.00	0.01	0.01	0.01	0.00	0.02
Ho	0.00	0.00	0.00	0.00	0.00	0.00	0.00	0.00	0.00	0.00
Er	0.01	0.00	0.00	0.01	0.00	0.00	0.00	0.01	0.00	0.01
Tm	0.00	0.00	0.00	0.00	0.00	0.00	0.00	0.00	0.00	0.00
Yb	0.01	0.03	0.07	0.02	0.04	0.00	0.02	0.04	0.00	0.03
Lu	0.00	0.00	0.00	0.00	0.00	0.00	0.00	0.01	0.01	0.00
Hf	0.27	0.23	0.32	0.31	0.24	0.36	0.12	0.23	0.13	0.19
Y	0.00	0.01	0.04	0.01	0.01	0.01	0.02	0.01	0.00	0.22
Zr	2.05	2.18	1.98	2.06	1.68	2.42	1.12	1.50	1.21	1.09
In	0.21	0.20	0.21	0.23	0.24	0.26	0.23	0.19	0.20	0.26
Hf	0.27	0.23	0.32	0.31	0.24	0.36	0.12	0.23	0.21	0.19
Rb	895	859	877	869	859	831	932	938	877	854
Sr	0.72	0.77	1.34	1.66	0.85	1.26	0.92	0.54	0.52	3.02
Ba	6.19	7.16	9.72	6.59	8.38	7.97	1.69	5.17	3.47	7.59
Cs	32.3	25.6	31.4	23.3	21.5	28.1	19.1	25.6	24.6	29.4
W	34.5	32.5	30.6	32.9	34.4	34.1	27.0	34.4	29.6	28.4
Bi	0.02	0.01	0.01	0.02	0.00	0.01	0.00	0.01	0.01	0.01
Be	9.10	7.65	8.67	8.38	11.9	10.3	8.96	9.31	9.32	9.36
B	26.6	26.8	25.6	26.2	26.7	26.9	29.5	23.4	24.0	20.8
Pb	5.31	5.71	5.05	5.35	5.72	6.02	5.66	5.16	5.36	5.31
K/Rb	105	109	107	109	112	114	101	99.1	107	109

Table 4
chemical compositions of beryl. Li_2O* and Cs_2O* are calculated by the trace element content of Li and Cs, BeO* is calculated is Be*= 3-Li·H_2O* is calculated by (0.84958 × Na_2O) + 0.8373.

Major elements (wt%)																				
Na_2O	0.68	0.68	0.57	0.62	0.63	0.67	0.59	0.57	0.63	0.64	0.69	0.63	0.65	0.69	0.68	0.62	0.56	0.62	0.60	0.60
MgO	0.56	0.56	0.57	0.56	0.51	0.51	0.53	0.49	0.59	0.34	0.29	0.16	0.25	0.59	0.39	0.60	0.22	0.62	0.55	0.54
Al_2O_3	17.13	16.93	16.96	17.08	17.08	16.89	17.03	17.16	17.12	17.58	17.87	18.01	17.87	17.12	17.49	16.92	17.67	16.91	17.14	17.24
SiO_2	66.78	66.06	66.17	66.11	66.18	66.11	66.08	66.33	66.32	66.86	67.22	67.03	67.18	66.41	67.03	66.40	66.63	66.24	66.51	66.61
FeO	0.82	0.72	0.78	0.78	0.77	0.78	0.84	0.75	0.67	0.41	0.37	0.30	0.33	0.64	0.37	0.81	0.35	0.84	0.75	0.71
Li_2O*	0.06	0.06	0.06	0.05	0.07	0.07	0.06	0.06	0.07	0.06	0.06	0.05	0.05	0.06	0.07	0.10	0.07	0.07	0.07	0.07
Cs_2O*	0.16	0.15	0.12	0.15	0.15	0.16	0.16	0.19	0.17	0.17	0.28	0.29	0.28	0.52	0.61	0.32	0.46	0.59	0.71	0.76
BeO*	13.81	13.66	13.69	13.69	13.68	13.66	13.67	13.71	13.70	13.83	13.91	13.88	13.91	13.73	13.86	13.67	13.76	13.69	13.74	13.75
H_2O*	1.42	1.42	1.32	1.36	1.37	1.41	1.34	1.32	1.37	1.38	1.42	1.37	1.39	1.42	1.42	1.36	1.31	1.36	1.35	1.35
Trace elements and rare earth elements (ppm)																				
Li	275	274	278	221	307	323	272	297	321	269	274	248	235	282	304	442	334	319	319	344
B	0.00	1.27	0.00	8.72	0.00	0.21	5.74	20.3	4.69	5.78	0.00	0.00	6.96	16.1	7.12	9.70	b.d.l.	7.17	b.d.l.	11.91
Zn	390	362	294	372	395	388	377	360	393	378	347	358	312	329	357	178	308	363	399	332
Ga	19.5	19.4	18.2	19.0	22.2	18.6	22.3	18.7	20.6	19.2	21.0	22.0	21.4	22.0	20.7	17.7	19.4	21.4	20.5	23.0
Ge	6.71	0.00	0.00	10.9	0.00	4.34	15.1	0.00	0.00	14.2	6.00	0.00	0.74	10.0	4.45	8.08	0.00	0.00	5.86	0.00
Rb	77.4	74.5	61.2	67.9	88.1	81.5	81.5	76.7	88.5	76.4	91.5	112	80.8	113	141	60.1	103	117	142	139
Sr	0.01	0.24	0.41	0.11	0.13	0.01	0.00	0.01	0.02	0.15	45.56	77.0	30.2	5.60	5.16	88.5	60.5	0.00	3.82	0.89
Y	0.01	0.09	0.27	0.00	0.00	0.11	0.10	0.00	0.00	0.00	0.00	0.10	0.00	0.01	0.11	0.03	0.00	0.03	0.03	0.00
Zr	0.10	0.00	0.01	0.00	0.00	0.00	0.08	0.00	0.18	0.06	0.37	0.70	0.00	0.00	0.00	0.00	0.00	0.71	0.00	1.13
Cs	1351	1323	1080	1314	1343	1376	1382	1657	1451	1509	2453	2603	2545	4624	5362	2875	4136	5257	6313	6757
Ta	0.03	0.38	0.49	0.16	0.00	0.01	0.05	0.01	0.00	0.01	0.36	0.15	0.40	0.48	0.11	0.28	0.30	0.40	0.11	1.21
Sc	5.02	11.5	12.3	8.66	9.40	8.00	15.0	7.40	8.91	11.11	1.89	2.07	4.27	4.75	1.56	7.06	6.85	6.04	6.95	9.57
V	0.58	0.00	0.23	0.97	1.17	0.00	1.43	1.24	2.13	0.00	0.00	0.00	0.40	0.71	0.31	0.50	0.00	0.00	0.72	1.86
Mo	1.62	1.41	0.00	0.00	2.72	0.41	0.86	0.14	0.00	0.00	0.02	0.00	0.44	0.00	0.06	0.00	0.66	0.00	0.13	0.07
Nb	0.35	0.04	0.53	0.23	0.00	0.27	0.01	0.00	0.29	0.01	0.07	0.14	0.34	0.26	0.12	0.15	0.16	0.21	0.00	0.40
As	1.83	0.00	2.23	0.00	0.00	0.00	0.00	2.51	0.05	1.52	0.00	1.65	3.32	0.00	0.21	0.00	1.38	0.00	0.00	0.46
Cr	0.02	29.0	75.6	104	17.4	102	80.0	15.5	0.00	17.7	0.00	9.91	24.7	68.9	0.00	12.9	18.4	31.6	1.96	37.2
Co	0.00	0.01	0.00	0.00	0.00	0.00	0.29	0.14	0.00	0.00	0.10	0.00	0.18	0.00	0.24	0.00	0.20	0.00	0.00	0.34
Ni	3.40	0.00	0.00	0.00	0.00	4.46	3.38	6.71	2.16	0.00	0.89	0.00	1.91	0.00	0.00	8.14	0.00	1.47	0.00	0.00
Cu	0.00	0.00	0.86	1.05	0.23	0.00	0.05	0.00	0.48	0.00	0.00	3.97	0.00	0.00	5.56	1.59	0.00	0.05	0.00	0.00
Cd	0.71	0.00	0.07	0.00	0.86	2.10	0.27	0.00	0.00	0.00	0.00	0.00	0.00	0.77	0.00	0.21	0.14	0.19	0.00	0.00
In	0.00	0.00	0.00	0.00	0.00	0.07	0.05	0.00	0.07	0.00	0.00	0.07	0.00	0.00	0.02	0.00	0.07	0.00	0.00	0.00
Sn	0.00	0.28	0.53	0.00	0.00	0.00	0.00	0.00	0.00	0.18	0.00	0.20	0.00	0.00	0.50	0.00	0.57	0.05	0.91	0.00
Sb	0.00	0.18	0.00	0.00	0.00	0.00	0.18	0.00	0.11	0.15	0.15	0.00	0.00	0.04	0.00	0.06	0.07	0.02	0.00	0.16
La	0.05	0.00	0.00	0.03	0.03	0.00	0.08	0.04	0.03	0.00	0.00	0.00	0.01	0.00	0.00	0.02	0.01	0.00	0.00	0.02
Ce	0.00	0.01	0.00	0.00	0.03	0.00	0.01	0.01	0.00	0.00	0.00	0.03	0.00	0.00	0.00	0.02	0.00	0.00	0.00	0.00
Pr	0.04	0.00	0.00	0.01	0.00	0.00	0.03	0.01	0.01	0.00	0.00	0.02	0.00	0.00	0.00	0.00	0.01	0.00	0.01	0.00
Nd	0.00	0.00	0.19	0.00	0.00	0.13	0.00	0.06	0.00	0.00	0.00	0.00	0.00	0.00	0.00	0.00	0.00	0.05	0.00	0.00
Sm	0.21	0.00	0.00	0.00	0.17	0.00	0.03	0.00	0.00	0.24	0.00	0.06	0.00	0.00	0.12	0.06	0.00	0.04	0.04	0.00
Eu	0.02	0.13	0.02	0.01	0.00	0.01	0.01	0.00	0.00	0.00	0.00	0.02	0.00	0.02	0.00	0.00	0.00	0.02	0.00	0.00
Gd	0.00	0.00	0.00	0.00	0.00	0.00	0.24	0.00	0.00	0.00	0.00	0.00	0.00	0.00	0.00	0.00	0.00	0.00	0.05	0.00
Tb	0.00	0.00	0.00	0.00	0.00	0.00	0.02	0.01	0.01	0.01	0.00	0.00	0.00	0.00	0.00	0.01	0.00	0.00	0.00	0.00
Dy	0.06	0.09	0.03	0.03	0.00	0.00	0.03	0.00	0.07	0.04	0.00	0.00	0.00	0.00	0.00	0.00	0.00	0.00	0.00	0.06
Ho	0.01	0.00	0.00	0.00	0.00	0.01	0.00	0.00	0.00	0.02	0.00	0.00	0.00	0.00	0.00	0.01	0.01	0.00	0.00	0.00
Er	0.00	0.00	0.00	0.07	0.00	0.00	0.00	0.00	0.00	0.03	0.00	0.00	0.00	0.00	0.00	0.00	0.00	0.00	0.00	0.02
Tm	0.00	0.02	0.00	0.00	0.00	0.00	0.00	0.01	0.05	0.00	0.01	0.00	0.00	0.00	0.00	0.01	0.00	0.00	0.00	0.00
Yb	0.04	0.00	0.13	0.00	0.10	0.00	0.00	0.00	0.05	0.00	0.00	0.03	0.00	0.00	0.00	0.00	0.10	0.03	0.04	0.00
Lu	0.00	0.00	0.01	0.00	0.02	0.00	0.01	0.01	0.00	0.00	0.00	0.00	0.00	0.01	0.00	0.00	0.01	0.00	0.00	0.00
Hf	0.00	0.02	0.00	0.02	0.00	0.05	0.05	0.00	0.03	0.00	0.07	0.00	0.04	0.00	0.02	0.04	0.00	0.14	0.02	0.07
W	0.00	0.03	0.00	0.00	0.00	0.10	0.06	0.03	0.03	0.03	0.05	0.03	0.19	0.13	0.00	0.23	0.04	0.00	0.00	0.06
Bi	0.06	0.01	0.05	0.00	0.00	0.00	0.03	0.00	0.02	0.00	0.00	0.05	0.02	0.00	0.02	0.01	0.01	0.00	0.00	0.04
Pb	0.82	0.00	0.44	0.81	1.21	0.51	0.19	6.46	0.00	2.31	0.00	0.56	0.91	0.00	0.00	0.72	4.07	0.00	0.00	0.00
Cs/Li	4.91	4.83	3.88	5.95	4.37	4.27	5.08	5.58	4.52	5.62	8.97	10.5	10.8	16.4	17.6	6.51	12.4	16.5	19.8	19.6
Cs/Rb	17.5	17.8	17.7	19.3	15.3	16.9	17.0	21.6	16.4	19.8	26.8	23.2	31.5	41.1	37.9	47.8	40.2	45.0	44.5	48.5

Table 5
chemical results of tourmaline. B_2O_3* and H_2O* are calculated on stoichiometry for B = 3 apfu and OH + F = 4 apfu.

Tourmaline	Tur 2	Tur 2	Tur 2	Tur 2	Tur 2	Tur 2	Tur 2	Tur 2	Tur 2	Tur 2	Tur 2	Tur 2	Tur 2	Tur 2	Tur 2	Tur 2	Tur 1	Tur 1	Tur 1	Tur 1	Tur 1	Tur 1	Tur 1	Tur 1
Major elements (wt%)																								
SiO_2	36.31	36.20	36.12	35.70	36.11	35.77	35.77	36.56	36.72	36.08	36.09	35.83	36.37	36.34	35.47	36.04	36.71	36.69	36.38	36.22	36.57	36.19	36.26	36.75
TiO_2	0.00	0.20	0.14	0.17	0.13	0.16	0.14	0.13	0.05	0.11	0.06	0.13	0.11	0.13	0.21	0.26	0.14	0.10	0.16	0.20	0.12	0.10	0.19	0.18
Al_2O_3	32.12	32.24	32.27	32.23	32.34	32.32	32.32	31.86	32.88	32.12	32.08	32.13	32.45	32.94	31.99	32.50	32.07	32.52	32.24	32.10	32.10	31.54	32.54	32.24
FeO	11.05	11.15	10.98	10.68	10.81	11.34	11.06	11.23	10.16	10.61	10.38	10.84	10.22	10.16	10.57	11.07	8.49	9.55	8.44	9.49	9.10	9.84	9.47	8.98
MnO	0.21	0.21	0.20	0.14	0.26	0.20	0.20	0.21	0.13	0.19	0.12	0.19	0.18	0.16	0.14	0.19	0.08	0.17	0.15	0.11	0.16	0.16	0.15	0.08
MgO	3.50	3.67	3.80	3.96	4.05	3.84	3.89	3.86	3.65	3.77	4.08	3.89	3.85	3.66	4.03	3.91	5.34	5.13	4.88	5.13	5.18	5.14	4.97	4.89
CaO	0.05	0.14	0.12	0.15	0.19	0.22	0.21	0.19	0.09	0.13	0.19	0.23	0.20	0.11	0.21	0.16	0.28	0.24	0.20	0.22	0.24	0.27	0.21	0.29
Na_2O	1.79	1.88	1.80	2.04	2.05	1.99	2.19	2.22	1.80	2.15	2.08	2.24	2.19	1.64	2.09	2.07	2.03	2.22	2.20	2.13	2.11	2.20	2.13	2.12
K_2O	0.05	0.05	0.03	0.03	0.03	0.04	0.04	0.07	0.03	0.06	0.05	0.07	0.03	0.06	0.07	0.04	0.08	0.05	0.06	0.06	0.05	0.03	0.05	0.04
F	0.17	0.38	0.11	0.00	0.06	0.07	0.00	0.00	0.07	0.45	0.14	0.00	0.00	0.00	0.09	0.01	0.19	0.47	0.09	0.43	0.36	0.05	0.32	0.00
Cl	0.00	0.00	0.00	0.00	0.00	0.00	0.03	0.00	0.00	0.00	0.00	0.00	0.00	0.00	0.00	0.00	0.00	0.00	0.00	0.00	0.00	0.00	0.00	0.00.
B_2O_3*	10.37	10.35	10.34	10.28	10.38	10.35	10.33	10.37	10.38	10.27	10.29	10.29	10.33	10.35	10.23	10.40	10.40	10.53	10.31	10.41	10.42	10.50	10.41	10.38
H_2O*	3.49	3.39	3.51	3.54	3.55	3.53	3.56	3.58	3.54	3.33	3.48	3.54	3.56	3.57	3.48	3.58	3.50	3.41	3.51	3.38	3.42	3.60	3.44	3.58
Total	85.76	85.96	85.53	85.09	86.03	85.92	85.85	86.31	85.56	85.48	85.22	85.56	85.60	85.20	84.86	86.26	85.33	86.94	84.77	85.93	86.58	85.79	86.21	85.77
Structural formula based on 31 total anions																								
X-site: Na	0.58	0.61	0.59	0.67	0.67	0.65	0.71	0.72	0.58	0.70	0.68	0.73	0.71	0.53	0.69	0.67	0.66	0.71	0.72	0.69	0.68	0.70	0.69	0.69
K	0.01	0.01	0.01	0.01	0.01	0.01	0.01	0.02	0.01	0.01	0.01	0.01	0.01	0.01	0.01	0.01	0.02	0.01	0.01	0.01	0.02	0.01	0.01	0.01
Ca	0.01	0.03	0.02	0.03	0.03	0.04	0.04	0.03	0.02	0.02	0.03	0.04	0.04	0.02	0.04	0.03	0.05	0.04	0.04	0.04	0.04	0.05	0.04	0.05
Vacancy	0.40	0.35	0.38	0.30	0.29	0.31	0.24	0.23	0.40	0.26	0.27	0.21	0.24	0.43	0.26	0.29	0.27	0.24	0.23	0.26	0.26	0.23	0.26	0.25
Y-site: Mg	0.87	0.92	0.95	1.00	1.01	0.96	0.98	0.96	0.91	0.95	1.03	0.98	0.97	0.92	1.02	0.97	1.33	1.26	1.23	1.28	1.29	1.27	1.24	1.22
Fe	1.55	1.57	1.54	1.51	1.51	1.59	1.56	1.57	1.42	1.50	1.47	1.53	1.44	1.43	1.50	1.55	1.19	1.32	1.19	1.32	1.27	1.36	1.32	1.26
V + W-site: OH	3.91	3.80	3.94	4.00	3.97	3.96	3.99	4.00	3.96	3.76	3.93	4.00	4.00	4.00	3.95	3.99	3.90	3.75	3.95	3.77	3.81	3.98	3.83	4.00
F	0.09	0.20	0.06	0.00	0.03	0.04	0.00	0.00	0.04	0.24	0.07	0.00	0.00	0.00	0.05	0.01	0.10	0.25	0.05	0.23	0.19	0.02	0.17	0.00
Cl	0.00	0.00	0.00	0.00	0.00	0.00	0.01	0.00	0.00	0.00	0.00	0.00	0.00	0.00	0.00	0.00	0.00	0.00	0.00	0.00	0.00	0.00	0.00	0.00
Mg/(Mg + Fe)	0.36	0.37	0.38	0.40	0.40	0.38	0.39	0.38	0.39	0.39	0.41	0.39	0.40	0.39	0.40	0.39	0.53	0.49	0.51	0.49	0.51	0.48	0.48	0.49
X/(X + Na)	0.41	0.37	0.40	0.31	0.31	0.32	0.25	0.24	0.40	0.27	0.28	0.22	0.26	0.45	0.27	0.30	0.29	0.25	0.24	0.27	0.27	0.25	0.28	0.27
Trace elements and rare earth elements (ppm)																								
La	0.35	0.48	0.35	0.46	0.70	0.66	0.43	0.47	0.63	0.86	0.19	3.68	0.72	0.24	0.32	0.37	0.64	0.60	0.77	0.86	0.76	0.76	0.38	0.36
Ce	0.54	0.61	0.55	0.77	1.05	1.18	0.66	0.74	0.82	1.15	0.30	7.75	0.44	0.28	0.47	0.45	0.69	0.74	0.88	0.89	1.18	1.13	0.56	0.35
Pr	0.03	0.05	0.04	0.07	0.07	0.07	0.06	0.06	0.06	0.08	0.03	0.73	0.14	0.04	0.03	0.06	0.03	0.04	0.05	0.05	0.08	0.09	0.05	0.03
Nd	0.11	0.10	0.06	0.23	0.21	0.17	0.11	0.16	0.16	0.23	0.06	2.18	0.58	0.13	0.07	0.11	0.07	0.09	0.09	0.08	0.24	0.20	0.08	0.07
Sm	0.00	0.01	0.00	0.03	0.01	0.05	0.01	0.00	0.06	0.04	0.00	0.56	0.17	0.05	0.02	0.05	0.00	0.02	0.00	0.06	0.00	0.01	0.02	0.05
Eu	0.00	0.00	0.01	0.00	0.03	0.00	0.00	0.00	0.03	0.02	0.00	0.00	0.00	0.00	0.02	0.03	0.00	0.01	0.01	0.00	0.03	0.00	0.00	0.04
Gd	0.01	0.00	0.17	0.28	1.61	0.57	0.00	0.18	0.00	0.77	0.56	0.00	1.54	0.00	0.00	0.00	0.27	0.00	0.34	0.26	0.26	0.22	0.00	0.41
Tb	0.00	0.00	0.00	0.00	0.00	0.01	0.00	0.00	0.00	0.01	0.00	0.12	0.06	0.01	0.01	0.00	0.00	0.00	0.00	0.00	0.00	0.00	0.00	0.00
Dy	0.00	0.00	0.00	0.01	0.02	0.06	0.00	0.00	0.03	0.04	0.02	1.02	0.34	0.01	0.02	0.05	0.00	0.00	0.01	0.02	0.00	0.01	0.01	0.00
Ho	0.00	0.00	0.00	0.00	0.00	0.00	0.00	0.00	0.01	0.01	0.00	0.26	0.05	0.01	0.00	0.00	0.00	0.00	0.00	0.00	0.00	0.00	0.00	0.00
Er	0.00	0.00	0.00	0.02	0.01	0.03	0.01	0.01	0.01	0.03	0.01	1.22	0.15	0.04	0.00	0.00	0.00	0.00	0.00	0.01	0.00	0.00	0.00	0.00
Tm	0.00	0.00	0.00	0.01	0.00	0.01	0.00	0.00	0.00	0.01	0.00	0.26	0.02	0.01	0.00	0.01	0.00	0.01	0.00	0.00	0.00	0.00	0.00	0.01
Yb	0.00	0.00	0.03	0.08	0.11	0.12	0.00	0.00	0.04	0.08	0.00	3.18	0.39	0.01	0.00	0.06	0.00	0.00	0.00	0.00	0.00	0.00	0.00	0.01
Lu	0.00	0.01	0.00	0.01	0.01	0.02	0.00	0.01	0.01	0.01	0.00	0.50	0.03	0.02	0.00	0.00	0.00	0.00	0.00	0.00	0.00	0.01	0.00	0.00
Hf	0.02	0.01	0.01	0.02	0.04	0.00	0.00	0.02	0.00	0.01	0.02	0.13	0.02	0.03	0.00	0.01	0.03	0.02	0.01	0.02	0.01	0.02	0.00	0.01
Ta	0.09	0.14	0.18	0.21	0.14	0.42	0.82	0.10	0.20	0.20	0.12	0.84	0.83	0.26	0.10	0.11	0.10	0.11	0.17	0.20	0.16	0.18	0.18	0.29
Y	0.01	0.05	0.01	0.17	0.06	0.22	0.01	0.00	0.33	0.43	0.13	0.30	0.21	0.70	0.20	0.23	0.02	0.02	0.05	0.07	0.05	0.07	0.07	0.07
Zr	0.07	0.06	0.08	0.11	0.15	0.21	0.09	0.07	0.14	0.26	0.10	1.97	0.29	0.27	0.14	0.12	0.06	0.11	0.09	0.12	0.11	0.12	0.04	0.09
Nb	0.11	0.17	0.23	0.93	0.35	1.83	0.64	0.29	0.80	1.12	0.34	1.06	0.77	0.91	0.32	0.43	0.25	0.29	0.40	0.51	0.45	0.75	0.43	0.21
W	0.01	0.00	0.02	0.17	0.02	0.43	0.00	0.00	0.21	0.20	0.05	0.46	1.83	0.14	0.02	0.03	0.02	0.02	0.03	0.07	0.03	0.12	0.14	0.05
Mo	0.06	0.01	0.03	0.09	0.12	0.14	0.00	0.03	0.11	0.02	0.06	0.12	0.14	0.07	0.01	0.04	0.03	0.01	0.08	0.04	0.05	0.05	0.01	0.03
Bi	0.01	0.01	0.00	0.02	0.01	0.01	0.02	0.01	0.07	0.23	0.11	0.15	1.00	0.35	0.10	0.13	0.01	0.00	0.01	0.00	0.01	0.01	0.02	0.00
Zn	849	824	924	859	905	790	1172	938	658	555	716	464	400	606	741	727	388	403	385	349	384	380	376	399
Ga	67.1	67.1	68.5	74.8	77.4	77.5	96.4	73.7	73.2	73.4	64.0	65.9	63.7	63.7	64.7	63.5	72.4	71.5	71.3	76.7	80.1	76.9	71.7	65.4
Li	22.9	22.9	21.7	25.6	23.0	30.3	29.9	27.9	32.2	25.4	19.5	20.8	20.3	27.4	19.6	37.3	22.1	24.3	21.9	26.1	24.0	21.8	28.6	24.6
Be	2.51	2.66	2.48	1.94	2.11	2.76	2.48	2.20	2.51	3.64	3.00	3.37	3.11	2.96	4.07	2.49	2.00	3.54	2.44	5.60	1.86	2.47	1.84	2.62

(*continued on next page*)

Table 5 (*continued*)

Tourmaline	Tur 2	Tur 2	Tur 2	Tur 2	Tur 2	Tur 2	Tur 2	Tur 2	Tur 2	Tur 2	Tur 2	Tur 2	Tur 2	Tur 2	Tur 1	Tur 1	Tur 1	Tur 1	Tur 1	Tur 1	Tur 1	Tur 1	Tur 1
Sc	6.04	6.15	6.19	5.92	6.30	6.27	6.62	7.20	6.16	6.51	6.92	7.09	6.89	6.19	6.35	6.73	5.80	5.83	5.83	6.94	5.68	5.65	6.08	5.95
V	1.59	1.60	1.58	1.97	2.04	0.97	1.09	0.92	1.12	1.02	0.94	1.04	1.18	0.76	0.69	1.00	1.91	2.10	2.17	2.08	1.88	2.00	1.89	1.47
Cr	0.00	0.53	0.59	0.73	0.41	0.74	0.00	0.34	1.38	0.83	0.76	2.62	3.85	0.38	1.99	0.73	0.44	0.07	0.36	0.21	0.95	0.49	0.00	0.00
Co	1.71	2.01	4.00	5.08	4.57	2.15	3.03	3.25	2.46	2.19	2.90	2.04	2.55	2.54	2.19	2.80	9.63	9.97	9.98	8.91	9.97	9.31	10.22	10.61
Ni	0.00	0.03	0.25	0.28	0.15	0.06	0.00	0.00	0.22	0.25	0.10	0.40	0.00	0.11	0.10	0.00	0.52	0.72	0.67	0.52	0.07	0.00	0.28	0.00
Cu	0.63	0.76	0.63	2.67	0.80	4.01	0.68	0.66	2.91	2.68	1.33	2.80	1.46	2.64	1.37	2.76	0.88	0.90	0.88	0.92	0.88	1.40	1.66	0.93
As	0.14	0.13	0.12	0.00	0.18	0.07	0.13	0.15	0.12	0.18	0.14	0.24	0.45	0.32	0.02	0.10	0.14	0.06	0.13	0.20	0.13	0.11	0.18	0.21
Sn	1.89	2.04	2.11	2.07	2.45	3.42	3.06	3.60	3.01	3.95	3.21	3.96	3.65	2.72	3.19	3.45	2.15	2.19	2.27	3.29	2.11	2.01	2.27	2.02
Ge	2.15	2.31	1.98	2.61	2.75	2.46	2.75	2.78	2.32	2.67	1.83	2.74	2.20	1.75	1.54	2.86	2.79	2.82	3.02	3.44	2.69	2.56	3.06	2.33
Cs	0.00	0.03	0.00	1.49	0.02	3.45	0.01	0.00	3.44	4.99	2.53	3.43	3.95	5.31	0.89	1.72	0.00	0.12	0.01	1.61	0.00	1.64	0.69	0.01
Cd	0.00	0.01	0.00	0.09	0.00	0.08	0.00	0.01	0.00	0.04	0.00	0.05	0.04	0.04	0.11	0.01	0.00	0.03	0.00	0.01	0.01	0.01	0.00	0.00
In	0.01	0.02	0.02	0.01	0.04	0.04	0.02	0.02	0.02	0.02	0.01	0.05	0.01	0.02	0.01	0.01	0.02	0.02	0.03	0.04	0.02	0.02	0.01	0.02
Sb	0.01	0.02	0.01	0.00	0.02	0.02	0.00	0.02	0.00	0.06	0.02	0.30	0.01	0.04	0.00	0.02	0.02	0.00	0.02	0.00	0.01	0.03	0.01	0.01
Ba	0.00	0.09	0.00	2.88	0.42	6.08	0.00	0.00	3.93	5.13	1.73	10.1	9.35	6.17	1.16	1.73	0.00	2.75	0.36	0.50	0.00	3.71	1.77	0.03
Pb	3.41	3.55	2.79	3.95	3.26	4.35	2.20	2.78	3.47	4.01	1.54	30.4	5.42	1.85	1.61	1.90	3.65	3.59	4.61	4.77	3.00	3.23	3.76	3.12
Rb	0.08	0.08	0.03	58.42	0.06	135	0.03	0.02	84.8	99.2	32.5	26.4	260	76.7	12.2	25.1	0.00	2.15	0.33	0.71	0.07	79.2	31.3	0.69
Sr	2.36	2.69	1.68	4.23	3.89	1.52	1.49	1.63	1.18	3.22	1.09	2.20	2.72	1.03	2.54	1.78	3.11	4.13	5.81	5.15	3.16	4.27	3.01	2.61

μm.

4. Results

4.1. $^{40}Ar/^{39}Ar$ dating of muscovite

The results of $^{40}Ar/^{39}Ar$ step-heating analysis of muscovite are presented in Table 1. The sample yielded a well-defined plateau age of 405.33 ± 3.38 Ma (2 σ; MSWD = 0.22), consisting of three contiguous steps that account for 77% of the total ^{39}Ar precipitated (Fig. 5A). Only three steps fit an isochron age, whereas the other steps contain excess argon (Fig. 5A).

4.2. U-pb dating of garnet

The U-Pb isotopic data of garnet from the Weiling pegmatite are shown in Table 2. All analyzed fractions have low U contents (0.30–3.60 ppm) and relatively low $^{206}Pb/^{204}Pb$ values (27.78–63.28). Therefore, the data are plotted on a Tera-Wasserburg diagram (Fig. 5B), which in contrast to the concordia diagram does not require a correction of the common Pb contribution. The data plot on the Tera-Wasserburg diagram near the $^{207}Pb/^{206}Pb$ intercept and show important excess scatter. Therefore, the age for garnet from the Weiling pegmatite has a relatively large error (464 ± 59 Ma, 2 σ; MSWD = 10.7; Fig. 5B). Nevertheless, despite the relatively large error, the garnet U-Pb age of the Weiling pegmatite shows that this pegmatite is distinctly older than the Mesozoic granites that gave rise to important Sn and W mineralization in the SCB.

4.3. Mineral chemistry of pegmatite-forming minerals

Chemical compositions of the pegmatitic minerals muscovite, beryl, tourmaline, garnet, and K-feldspar are given in Tables 3, 4, 5, 6, and 7.

The composition of muscovite is relatively homogeneous with 46.57–47.87 wt% SiO_2, 33.37–34.45 wt% Al_2O_3, 7.49–10.19 wt% K_2O, 2.46–3.56 wt% FeO, 0.64–0.74 wt% MgO, and 0.17–0.60 wt% Na_2O (Table 3). The variation of the K_2O contents indicates that muscovite is locally altered. Muscovite has high contents of Rb (831–938 ppm), Nb (139–319 ppm), Cs (19.1–32.3 ppm), W (27.0–34.4 ppm), B (20.8–29.5 ppm), Be (7.65–11.9 ppm), Sn (51.1–67.0 ppm), Ta (8.36–30.5 ppm), Li (20.6–33.8 ppm), Sc (14.5–20.6 ppm), Zn (67.3–87.6 ppm), and Ga (100–107 ppm) and high K/Rb ratios (99.1–114). The contents of other trace elements and the rare earth elements are low.

The composition of beryl shows little variation with 66.06–67.22 wt % SiO_2, 16.89–18.01 wt% Al_2O_3, and 13.66–13.91 wt% BeO (calculated). The contents of Na_2O (0.56–0.69 wt%), FeO (0.30–0.84 wt%), and MgO (0.16–0.62 wt%) are low. Calculated H_2O contents (using the equation $H_2O = (0.84958 \times Na_2O) + 0.8373$; Giuliani et al., 1997) range from 1.31 to 1.42 wt%. The contents of trace elements are variable and – in part – high: Cs (1080–6757 ppm), Li (221–442 ppm), Zn (178–399 ppm), Ga (17.7–23.0 ppm), Rb (60.1–142 ppm), Sc (1.56–15.0 ppm), Ge (b.d.l.–15.1 ppm), and Cr (b.d.l.–104 ppm). The contents of other trace elements and the rare earth elements are very low. The Cs/Li and Cs/Rb ratios range from 3.88 to 19.8 and 15.3–48.5, respectively (Table 4).

Some tourmaline crystals have homogeneous compositions (Fig. 4B), whereas others show alteration (Fig. 4C). Two groups of tourmaline are distinguished, Tur 1 has Mg/(Mg + Fe) ratios of 0.48 to 0.53, which plots on the schorl-dravite boundary, whereas Tur 2 has Mg/(Mg + Fe) ratios of 0.36 to 0.41, which is typical for schorl (Fig. 8A; Table 5). Tur 2 has more Zn and less Co than Tur 1 (Fig. 8B). Concentrations of most trace elements (Be, Sc, V, Co, Sn, Ge, Sr) in tourmaline from the Weiling pegmatite show median concentrations of 1 to 11 ppm. The Li and Ga contents are slightly higher (20–90 ppm) and the Zn contents are markedly higher (349–1172 ppm). According to the classification of Henry et al. (2011), Tur 1 and Tur 2 both belong to the alkali group characterized by a Na + K site (Fig. 8C). In the Al-Fe-Mg ternary diagram of Henry et al. (1985), the composition of Tur 1 falls into the field of

Table 6
chemical compositions of garnet.

Garnet	Fine-grained Garnet														Coarse-grained Garnet								
	1	2	3	4	5	6	7	8	9	10	11	12	13	14	1	2	3	4	5	6	7	8	9
Major elements (wt%)																							
Na_2O	0.00	0.04	0.04	0.04	0.01	0.07	0.04	0.05	0.04	0.00	0.06	0.04	0.11	0.05	0.09	0.01	0.06	0.05	0.03	0.00	0.04	0.04	0.06
MgO	2.04	2.00	1.97	1.90	1.88	2.03	2.01	1.75	2.00	1.97	1.98	1.85	1.87	1.87	1.01	1.00	1.00	0.96	0.91	0.89	0.95	0.97	0.95
Al_2O_3	20.18	20.48	20.51	19.97	20.25	20.48	20.50	19.36	20.32	20.33	20.37	20.17	20.25	20.21	20.57	20.55	20.34	20.59	20.41	19.54	20.40	20.30	20.57
SiO_2	36.84	37.46	37.39	36.65	37.13	37.21	37.34	35.87	37.22	36.95	37.02	36.69	36.70	36.84	36.06	36.20	36.35	36.29	36.17	34.14	36.39	36.20	36.48
FeO	26.09	25.73	26.43	25.96	25.58	25.79	25.37	25.46	25.87	25.75	24.93	25.58	25.41	25.37	19.84	20.08	20.31	20.05	20.06	20.17	20.24	20.17	20.18
MnO	14.38	14.28	14.44	14.56	15.09	15.08	15.06	15.41	15.19	14.88	15.06	15.27	15.20	15.40	23.03	23.28	23.09	22.99	23.07	22.99	22.96	22.83	22.47
TiO_2	0.01	0.01	0.00	0.07	0.02	0.00	0.00	0.02	0.00	0.00	0.02	0.00	0.05	0.00	0.02	0.06	0.04	0.03	0.04	0.05	0.07	0.02	0.04
CaO	0.37	0.33	0.46	0.48	0.47	0.48	0.54	0.52	0.27	0.44	0.48	0.39	0.41	0.44	0.19	0.22	0.28	0.19	0.19	0.22	0.21	0.20	0.23
K_2O	0.00	0.00	0.00	0.01	0.01	0.01	0.03	0.03	0.00	0.00	0.00	0.00	0.03	0.00	0.02	0.01	0.01	0.01	0.03	0.03	0.01	0.00	0.04
Total	99.96	100.42	101.28	99.68	100.45	101.17	100.92	98.48	100.97	100.36	99.93	100.26	100.32	100.17	100.89	101.44	101.58	101.21	100.90	98.03	101.33	100.74	101.05
X_{alm}	0.57	0.58	0.58	0.58	0.57	0.56	0.56	0.55	0.56	0.57	0.56	0.56	0.56	0.56	0.43	0.43	0.43	0.43	0.43	0.42	0.43	0.43	0.44
X_{sps}	0.33	0.33	0.33	0.33	0.34	0.34	0.34	0.36	0.35	0.34	0.35	0.35	0.35	0.35	0.52	0.53	0.52	0.52	0.53	0.53	0.52	0.52	0.51
X_{pro}	0.08	0.08	0.08	0.08	0.07	0.08	0.08	0.07	0.08	0.08	0.08	0.08	0.08	0.08	0.04	0.04	0.04	0.04	0.04	0.04	0.04	0.04	0.04
X_{grs}	0.01	0.01	0.01	0.01	0.01	0.01	0.02	0.02	0.01	0.01	0.01	0.01	0.01	0.01	0.01	0.01	0.01	0.01	0.01	0.01	0.01	0.01	0.01
X_{adr}	0.00	0.00	0.00	0.00	0.00	0.00	0.00	0.00	0.00	0.00	0.00	0.00	0.00	0.00	0.00	0.00	0.00	0.00	0.00	0.00	0.00	0.00	0.00
MnO/(FeO + MgO)	0.51	0.51	0.51	0.52	0.55	0.54	0.55	0.57	0.55	0.54	0.56	0.56	0.56	0.57	1.10	1.10	1.08	1.09	1.10	1.09	1.08	1.08	1.06
Trace elements and rare earth elements (ppm)																							
La	0.01	0.00	0.00	0.01	0.00	0.00	0.00	0.00	0.00	0.00	0.00	0.19	0.00	0.01	0.04	0.00	0.00	0.00	0.01	0.00	0.00	0.00	0.00
Ce	0.02	0.01	0.01	0.04	0.00	0.00	0.00	0.00	0.00	0.00	0.00	0.81	0.00	0.00	0.00	0.01	0.00	0.00	0.00	0.00	0.00	0.00	0.00
Pr	0.01	0.01	0.00	0.01	0.00	0.00	0.00	0.00	0.00	0.00	0.01	0.16	0.00	0.00	0.01	0.00.	0.00	0.00	0.01	0.00	0.00	0.00	0.01
Nd	0.03	0.05	0.02	0.07	0.02	0.01	0.03	0.02	0.02	0.00	0.03	0.68	0.02	0.01	0.22	0.00	0.06	0.05	0.03	0.20	0.08	0.09	0.08
Sm	0.29	0.40	0.12	0.12	0.08	0.07	0.14	0.15	0.15	0.07	0.15	0.46	0.18	0.08	0.46	0.68	0.62	0.52	0.58	0.52	0.62	0.67	0.78
Eu	0.05	0.07	0.01	0.02	0.00	0.04	0.00	0.00	0.01	0.00	0.00	0.08	0.02	0.00	0.02	0.01	0.01	0.00	0.01	0.01	0.00	0.00	0.01
Gd	3.88	4.78	0.93	1.31	1.08	1.34	1.35	1.63	0.44	0.70	0.74	2.14	1.35	0.00	3.89	3.96	4.45	4.17	3.92	3.17	3.82	4.22	3.84
Tb	2.89	3.18	0.62	0.79	1.03	1.32	1.19	1.19	0.41	0.83	0.50	1.23	0.52	0.38	2.25	2.34	2.30	2.19	2.24	2.17	2.08	2.27	2.25
Dy	40.8	45.9	6.86	12.7	15.6	19.4	16.3	15.6	4.09	11.7	5.59	19.4	5.24	4.08	17.3	19.5	19.2	18.3	18.1	17.6	18.5	18.7	19.4
Ho	12.0	13.0	1.47	4.87	4.84	5.75	4.26	4.11	0.77	3.02	1.19	6.06	1.15	0.92	1.84	2.15	1.98	2.18	2.15	1.75	1.98	1.98	2.08
Er	52.5	56.8	5.71	24.8	19.7	23.8	17.6	16.3	2.68	11.8	4.55	26.0	4.70	3.97	3.78	4.00	3.79	3.51	4.01	3.40	3.68	3.72	3.88
Tm	14.4	15.5	1.56	6.35	4.62	5.56	4.25	3.82	0.65	2.76	1.18	6.57	1.25	1.13	0.44	0.54	0.57	0.59	0.63	0.60	0.57	0.55	0.50
Yb	155	169	16.0	70.7	46.4	56.1	43.3	37.8	6.98	25.6	12.8	68.4	13.9	13.0	3.76	4.44	3.41	4.10	4.10	3.35	3.48	3.50	3.71
Lu	24.7	26.5	2.54	13.4	6.23	8.76	6.26	5.40	0.81	3.55	1.80	10.2	2.17	2.03	0.30	0.32	0.31	0.25	0.30	0.24	0.25	0.26	0.27
HREE	306	335	35.6	135	99.4	122	94.5	85.9	16.8	60.0	28.3	140	30.3	25.5	33.5	37.2	36.0	35.3	35.5	32.3	34.3	35.2	35.9
Li	141	140	94.3	41.3	46.0	62.6	85.8	77.1	200	56.3	61.2	40.6	140	150	250	258	252	258	254	262	259	254	246
Be	0.21	0.13	0.03	0.73	0.00	0.03	0.02	0.02	0.01	0.00	0.10	1.00	0.01	0.03	0.21	0.17	0.51	0.00	0.00	0.12	0.36	0.00	0.16
B	20.3	18.5	18.5	15.1	13.5	13.4	13.5	12.5	13.9	13.6	9.79	13.7	14.2	13.5	5.11	0.00	2.73	0.00	0.17	3.19	0.00	0.00	1.67
Sc	17.7	24.5	22.9	27.6	30.3	26.9	24.1	25.8	21.2	25.9	23.1	32.9	20.8	19.0	5.11	4.81	5.25	4.42	5.83	4.06	5.53	5.24	4.77
V	0.19	0.19	0.16	0.25	0.20	0.27	0.25	0.20	0.11	0.20	0.12	0.23	0.04	0.07	0.41	0.63	0.29	0.58	0.47	0.16	0.66	0.45	0.86
Cr	0.90	0.27	0.90	0.30	0.17	0.50	0.09	0.31	0.37	0.42	1.05	0.67	0.64	0.00	9.78	6.94	1.49	0.00	0.60	0.00	0.00	0.00	0.40
Co	3.55	2.95	3.80	4.11	4.39	4.57	4.30	4.44	4.34	4.39	3.24	4.34	4.37	4.53	1.56	0.21	0.32	1.22	1.01	0.88	0.00	0.00	1.16
Ni	0.66	0.23	0.13	0.09	0.12	0.07	0.03	0.04	0.00	1.20	0.08	0.10	0.01	0.03	0.00	0.00	0.00	0.05	0.11	0.72	0.00	0.08	0.00
Cu	0.00	0.00	0.66	0.20	0.03	0.01	0.03	0.09	0.14	0.09	0.01	0.35	0.07	0.07	1.20	0.00	0.00	0.00	0.00	0.01	0.44	0.00	0.70
Zn	97.7	84.7	97.2	92.9	97.1	94.8	95.0	96.8	97.2	95.7	70.1	90.7	96.6	95.9	149	151	160	149	156	159	156	159	161
Ga	26.1	19.2	14.3	12.5	11.7	14.0	17.3	16.6	30.0	15.2	14.3	11.5	24.4	25.7	30.0	24.7	25.0	23.2	26.6	25.4	25.9	25.4	26.4
Ge	50.4	48.4	29.5	32.1	41.6	47.0	54.1	58.0	73.7	55.7	39.7	36.8	67.1	68.4	93.1	92.8	94.7	103	98.5	99.2	113	98.6	101
As	0.00	0.00	0.43	0.33	0.27	0.22	0.32	0.20	0.34	0.21	0.20	0.46	0.26	0.26	0.61	0.00	0.62	0.00	0.74	0.80	0.00	0.00	2.98
Rb	0.06	0.11	12.3	35.0	0.04	0.00	0.03	0.00	0.00	0.02	0.07	1.92	0.00	0.00	26.89	0.03	0.14	0.00	0.00	0.04	0.08	0.15	0.07
Sr	0.00	0.00	0.45	0.35	0.05	0.07	0.05	0.04	0.02	0.02	0.03	0.17	0.01	0.04	0.43	0.06	0.01	0.04	0.00	0.00	0.00	0.03	0.00
Y	107	85.8	124	107	134	155	137	132	35.2	96.1	47.0	173	45.4	38.4	111	117	118	122	111	119	118	117	106
Zr	6.69	3.80	6.11	4.75	2.91	5.37	6.63	6.53	19.0	3.86	5.31	3.90	12.5	11.3	18.5	18.9	19.9	19.3	18.0	19.6	19.7	20.0	20.6
Nb	2.42	0.61	1.28	0.27	0.00	0.00	1.49	0.92	6.18	0.09	1.86	0.71	3.34	1.70	3.81	3.14	3.35	3.64	2.59	4.02	3.64	3.35	3.07
Mo	4.22	3.70	5.28	4.31	4.32	4.55	4.26	4.37	4.32	4.33	3.22	4.76	4.50	4.34	1.90	2.18	2.30	1.40	2.50	2.86	1.68	2.05	1.62

(*continued on next page*)

Table 6 (*continued*)

Garnet	Fine-grained Garnet													Coarse-grained Garnet								
	1	2	3	4	5	6	7	8	9	10	11	12	13	14	1	2	3	4	5	6	7	8	9
Cd	5.06	4.18	5.50	5.50	6.47	5.93	6.13	6.36	6.53	5.90	4.56	6.24	6.50	7.54	9.99	9.41	9.81	11.7	10.6	10.0	11.5	10.6	10.7
In	0.00	0.04	0.05	0.03	0.02	0.02	0.02	0.03	0.09	0.03	0.05	0.03	0.06	0.07	0.10	0.09	0.01	0.04	0.01	0.04	0.04	0.00	0.03
Sb	0.23	0.06	0.03	0.02	0.00	0.00	0.00	0.00	0.00	0.00	0.00	0.04	0.00	0.00	0.08	0.00	0.07	0.00	0.00	0.00	0.10	0.03	0.00
Cs	0.01	0.02	0.64	2.08	0.00	0.01	0.03	0.01	0.00	0.00	0.00	0.00	0.00	0.01	1.70	0.01	0.00	0.00	0.01	0.00	0.02	0.02	0.00
Hf	0.53	0.19	0.23	0.14	0.12	0.14	0.37	0.32	1.54	0.13	0.32	0.17	0.88	0.89	1.37	1.63	1.47	1.64	1.32	1.80	1.57	1.48	1.59
Ta	0.32	0.75	0.28	0.09	0.01	0.02	1.21	0.69	0.75	0.11	1.29	0.44	3.66	3.86	5.25	5.48	5.22	5.33	4.44	5.71	5.21	5.48	5.13
W	0.02	0.07	0.29	0.32	0.03	0.05	0.05	0.02	0.01	0.02	0.04	0.30	0.00	0.00	0.09	0.10	0.09	0.13	0.04	0.03	0.08	0.02	0.00
Bi	0.04	0.05	0.00	0.00	0.00	0.00	0.01	0.00	0.01	0.01	0.00	0.00	0.01	0.01	0.00	0.02	0.02	0.00	0.05	0.03	0.02	0.03	0.05
Pb	0.03	0.03	0.38	0.16	0.02	0.00	0.00	0.00	0.12	0.05	0.04	0.00	0.02	0.22	0.13	0.00	0.00	0.01	0.02	0.02	0.06	0.02	0.01
Y/Ho	12.8	11.8	60.5	46.3	36.1	28.3	31.3	30.2	90.7	44.6	73.5	29.8	70.6	97.7	16.1	15.5	15.8	16.6	16.1	15.8	17.5	15.9	16.2
Zr/Hf	0.17	0.15	1.66	0.37	0.55	0.46	0.59	0.67	3.70	1.01	1.96	0.37	1.83	1.96	5.28	4.52	5.95	4.89	4.90	6.02	5.82	5.76	5.44

metapelites and metapsammites with coexisting Al-saturating phases, whereas the composition of Tur 2 falls in the field of Li-poor granitoids and associated pegmatites and aplites (Fig. 8D). Both groups of tourmaline have similar REE patterns with LREE enrichment and positive Eu anomalies (Fig. 8E).

Garnet from the Weiling pegmatite forms almandine-spessartine solid solutions (Table 6) and is characterized by low CaO contents (0.19–0.54 wt%) and variable, but high FeO and MnO contents: 19.84–20.31 wt% and 14.28–15.41 wt% for the coarse-grained garnet, 24.93–26.43 wt% and 22.47–23.28 wt% for the fine-grained garnet (Fig. 9A, B), respectively. Such garnet is typical for peraluminous (S-type) granites (Dutrow and Henry, 2011; Harangi et al., 2001). Apart from higher MnO contents, coarse-grained garnet also has higher Li, Zn, Zr, Ge, Cd, Ta, and Hf contents, higher MnO/(MnO + FeO) and Zr/Hf ratios, lower FeO, B, Mo, Co, Lu, Sc, and HREE contents, and lower Y/Ho ratios than garnet from the fine-grained layer (Fig. 9A-J; Table 6). Coarse-grained garnet has a marked enrichment of MREE, whereas fine-grained garnet has a strongly negative Eu anomaly and a marked enrichment of HREE (Fig. 9K). Both types of garnet have low Be, V, Cr, Ni, Cu, As, Sb, Cs, W, Bi, and Pb contents (Table 6).

The composition of K-feldspar shows only little variation with 64.16–66.78 wt% SiO_2, 17.12–18.80 wt% Al_2O_3, 15.18–17.30 wt% K_2O, and 0.53–1.12 wt% Na_2O. K-feldspar has relatively low contents of Li (0.39–11.8 ppm), Be (1.45–5.44 ppm), B (4.33–10.4 ppm), Sc (4.07–5.12 ppm), Cu (0.25–2.79 ppm), Zn (0.36–11.2 ppm), Ga (9.34–30.5 ppm), Ge (2.05–3.84 ppm), Rb (458–533 ppm), Sr (11.9–74.0 ppm), Sn (0.24–4.58 ppm), Cs (20.4–54.5 ppm), Ba (13.2–227 ppm), Pb (57.4–156 ppm), and high K/Rb ratios (206–296) (Table 7).

4.4. Boron isotopic composition of tourmaline

Tourmaline B isotope data are shown in Table 8 and Fig. 10. The $\delta^{11}B$ values fall in a narrow range from –12.8 ‰ to –9.5 ‰, which is close to the average boron isotopic composition of continental crust (–10 ± 3 ‰) (Marschall and Jiang, 2011). There is no difference between $\delta^{11}B$ values of Tur 1 (–12.4 ‰ to –10.8 ‰) and Tur 2 (–12.8 ‰ to –9.5 ‰). Furthermore, the core and rim of tourmaline crystals do not show any difference in $\delta^{11}B$ isotope data.

4.5. Neodymium isotopic composition of Weiling pegmatite

The Nd isotopic compositions of garnet and feldspar from the Weiling pegmatite are shown in Table 9 and Fig. 11. Garnet contains abundant small apatite inclusions, which results in higher Sm and Nd contents and markedly lower $^{147}Sm/^{144}Nd$ ratios than typical garnet. Thus, the ε_{Nd} (t) values of the garnet samples may reflect the Nd isotopic composition of apatite shielded by garnet rather than garnet itself. The $\varepsilon_{Nd}(t)$ values of –12.0 and –11.4 for garnet (plus apatite) and –13.0 and –12.8 for K-feldspar fall into the range typical for average Proterozoic crust of the South China Block, implying that the Weiling pegmatite formed from partial melting of Mesoproterozoic crust. The Early Paleozoic as well as the strongly mineralized Triassic and Jurassic granites of the SCB could be derived from the same protoliths (Fig. 11).

4.6. Fluid inclusion data

Based on phase composition and phase proportion at 25 ℃, there are three types of fluid inclusions in quartz and beryl samples from the coarse-grained pegmatite.

(1) L-type inclusions: Liquid-rich inclusions are the most abundant type of fluid inclusions in quartz and beryl. These oval to irregular inclusions typically have 2–10 μm diameter (Fig. 12A-D).

(2) V-type inclusions: Vapor-rich inclusions are relatively uncommon. At 25 °C, the vapor bubble occupies 50–80 vol% of the volume of the fluid inclusion (Fig. 12A, D).

Table 7
chemical compositions of K-feldspar.

Major elements (wt%)															
Na_2O	0.66	0.53	0.65	0.78	0.66	0.66	1.12	0.64	0.81	0.85	0.58	0.57	0.89	0.71	0.74
MgO	0.00	0.01	0.01	0.00	0.00	0.00	0.00	0.00	0.00	0.00	0.00	0.00	0.00	0.00	0.00
Al_2O_3	18.34	18.47	18.57	17.12	18.28	18.36	17.50	17.63	18.53	18.01	18.80	17.63	17.97	17.16	17.58
SiO_2	65.70	65.51	65.26	66.78	65.23	65.58	65.19	65.68	65.71	65.29	64.16	65.28	65.09	65.85	65.49
K_2O	15.81	16.06	15.78	15.18	15.30	15.48	15.32	16.17	16.52	16.42	17.30	16.59	16.76	16.26	16.64
CaO	0.02	0.02	0.00	0.04	0.05	0.01	0.05	0.02	0.02	0.04	0.02	0.01	0.02	0.05	0.03
FeO	0.00	0.00	0.03	0.01	0.01	0.01	0.02	0.01	0.01	0.01	0.01	0.01	0.02	0.03	0.03
Total	100.54	100.61	100.29	99.95	99.57	100.12	99.25	100.17	101.62	100.66	100.88	100.09	100.76	100.09	100.55
Trace and rare earth elements (ppm)															
Li	0.82	0.52	0.81	11.8	0.72	0.59	0.83	0.64	1.03	0.39	1.04	0.55	0.75	0.86	0.68
Be	3.57	3.38	4.14	5.44	4.62	1.71	1.46	1.49	1.47	1.59	1.63	1.51	1.45	1.58	1.65
B	5.05	4.52	4.44	10.4	4.33	5.63	5.81	6.27	6.49	5.93	5.50	5.79	5.47	5.23	5.31
Sc	4.42	4.64	4.62	4.82	4.63	4.07	4.46	4.82	4.51	4.22	4.47	5.12	4.51	4.08	4.45
V	0.00	0.00	0.02	0.76	0.00	0.00	0.00	0.00	0.00	0.00	0.00	0.00	0.00	0.03	0.05
Cr	0.37	0.71	1.10	0.00	0.71	1.05	0.04	1.04	0.00	1.00	2.09	1.04	0.67	0.00	0.12
MnO	0.00	0.00	0.00	0.03	0.00	0.00	0.00	0.00	0.00	0.00	0.00	0.00	0.00	0.00	0.00
Co	0.00	0.06	0.02	0.29	0.18	0.09	0.17	0.11	0.00	0.00	0.04	0.00	0.22	0.07	0.00
Ni	0.00	0.21	0.15	0.22	0.18	0.66	0.01	0.52	0.00	0.28	0.43	0.35	0.48	0.00	0.43
Cu	0.51	1.05	0.59	0.86	0.54	1.09	0.73	2.79	0.75	0.25	1.62	2.14	1.80	0.51	0.28
Zn	1.13	0.68	1.09	11.2	0.81	0.49	0.36	0.56	0.55	0.77	1.78	1.31	1.15	1.15	0.71
Ga	14.6	12.1	16.2	30.5	15.6	16.3	16.2	15.3	16.8	13.6	12.1	11.0	9.61	9.34	11.5
Ge	3.84	3.51	3.67	2.07	3.64	2.86	2.54	2.66	2.49	2.05	2.35	2.49	2.17	2.30	2.16
As	0.00	0.00	0.00	0.00	0.00	0.00	0.00	0.00	0.00	0.00	0.00	0.00	0.00	0.00	0.00
Rb	458	528	460	518	482	479	486	497	509	498	473	533	515	533	489
Sr	74.0	39.9	35.2	48.3	37.2	13.7	12.5	13.5	11.9	25.3	24.5	20.5	15.5	16.1	18.9
Y	0.24	0.05	0.04	0.19	0.06	0.12	0.02	0.04	0.01	0.05	0.08	0.07	0.05	0.08	0.01
Zr	0.00	0.00	0.02	0.04	0.00	0.00	0.00	0.02	0.00	0.00	0.01	0.01	0.01	0.00	0.00
Nb	0.01	0.01	0.01	2.98	0.01	0.02	0.00	0.01	0.00	0.02	0.01	0.01	0.01	0.02	0.00
Mo	0.02	0.00	0.02	0.05	0.04	0.01	0.00	0.01	0.01	0.01	0.00	0.03	0.01	0.04	0.00
Cd	0.02	0.02	0.00	0.04	0.01	0.08	0.00	0.00	0.04	0.00	0.04	0.01	0.00	0.03	0.00
In	0.00	0.00	0.00	0.02	0.00	0.00	0.00	0.00	0.01	0.00	0.00	0.00	0.00	0.00	0.00
Sn	0.36	0.28	0.34	4.58	0.31	0.38	0.39	0.56	0.32	0.41	0.44	0.36	0.52	0.39	0.24
Sb	0.03	0.00	0.00	0.02	0.00	0.07	0.04	0.02	0.00	0.01	0.00	0.00	0.04	0.01	0.01
Cs	39.9	34.1	26.6	20.4	45.7	35.2	41.5	38.4	43.9	46.0	45.8	47.6	40.2	34.7	54.5
Ba	115	134	123	227	107	26.2	13.2	23.8	13.6	64.1	35.5	44.0	44.3	33.4	44.5
La	0.06	0.04	0.04	0.04	0.05	0.25	0.08	0.12	0.06	0.07	0.09	0.10	0.09	0.09	0.08
Ce	0.14	0.05	0.06	0.07	0.05	0.27	0.04	0.12	0.03	0.09	0.11	0.14	0.12	0.17	0.05
Pr	0.01	0.01	0.01	0.01	0.00	0.02	0.01	0.02	0.00	0.01	0.01	0.01	0.02	0.02	0.00
Nd	0.10	0.04	0.02	0.00	0.00	0.09	0.00	0.04	0.01	0.03	0.04	0.03	0.02	0.02	0.01
Sm	0.06	0.02	0.00	0.01	0.00	0.06	0.01	0.00	0.00	0.02	0.00	0.02	0.03	0.02	0.01
Eu	0.11	0.01	0.05	0.08	0.00	0.02	0.05	0.05	0.07	0.00	0.08	0.05	0.05	0.02	0.06
Gd	0.32	0.00	0.17	0.16	0.00	0.00	0.00	0.00	0.96	0.00	0.58	0.76	0.22	0.87	0.15
Tb	0.00	0.00	0.00	0.00	0.00	0.00	0.00	0.00	0.00	0.00	0.00	0.00	0.00	0.00	0.00
Dy	0.05	0.00	0.00	0.02	0.01	0.02	0.00	0.00	0.02	0.00	0.01	0.00	0.00	0.01	0.01
Ho	0.01	0.00	0.00	0.00	0.00	0.01	0.00	0.00	0.00	0.00	0.00	0.00	0.00	0.00	0.00
Er	0.00	0.00	0.01	0.02	0.03	0.01	0.00	0.01	0.00	0.00	0.00	0.01	0.00	0.01	0.00
Tm	0.00	0.00	0.01	0.00	0.00	0.00	0.00	0.00	0.00	0.00	0.00	0.00	0.00	0.00	0.00
Yb	0.05	0.03	0.02	0.00	0.03	0.03	0.05	0.03	0.00	0.07	0.02	0.00	0.03	0.01	0.10
Lu	0.00	0.01	0.01	0.01	0.00	0.00	0.00	0.00	0.01	0.00	0.00	0.00	0.00	0.00	0.00
Hf	0.00	0.00	0.00	0.00	0.01	0.00	0.02	0.01	0.01	0.00	0.02	0.00	0.00	0.00	0.00
Ta	0.04	0.01	0.02	0.60	0.03	0.01	0.01	0.02	0.00	0.01	0.01	0.01	0.03	0.03	0.01
W	0.02	0.01	0.00	1.27	0.00	0.23	0.04	0.03	0.01	0.00	0.00	0.03	0.03	0.05	0.02
Bi	0.02	0.01	0.02	0.03	0.01	0.00	0.00	0.01	0.00	0.01	0.01	0.01	0.01	0.00	0.00
Pb	138	127	81.3	57.4	112	88.1	100	95.7	103	129	149	102	111	116	156
Th	0.00	0.00	0.00	0.00	0.00	0.04	0.00	0.01	0.00	0.00	0.01	0.02	0.01	0.02	0.00
U	0.02	0.02	0.05	3.98	0.03	0.07	0.03	0.05	0.02	0.15	0.11	0.07	0.04	0.08	0.02
K/Rb	296	238	275	206	266	265	276	276	267	288	291	261	262	259	269

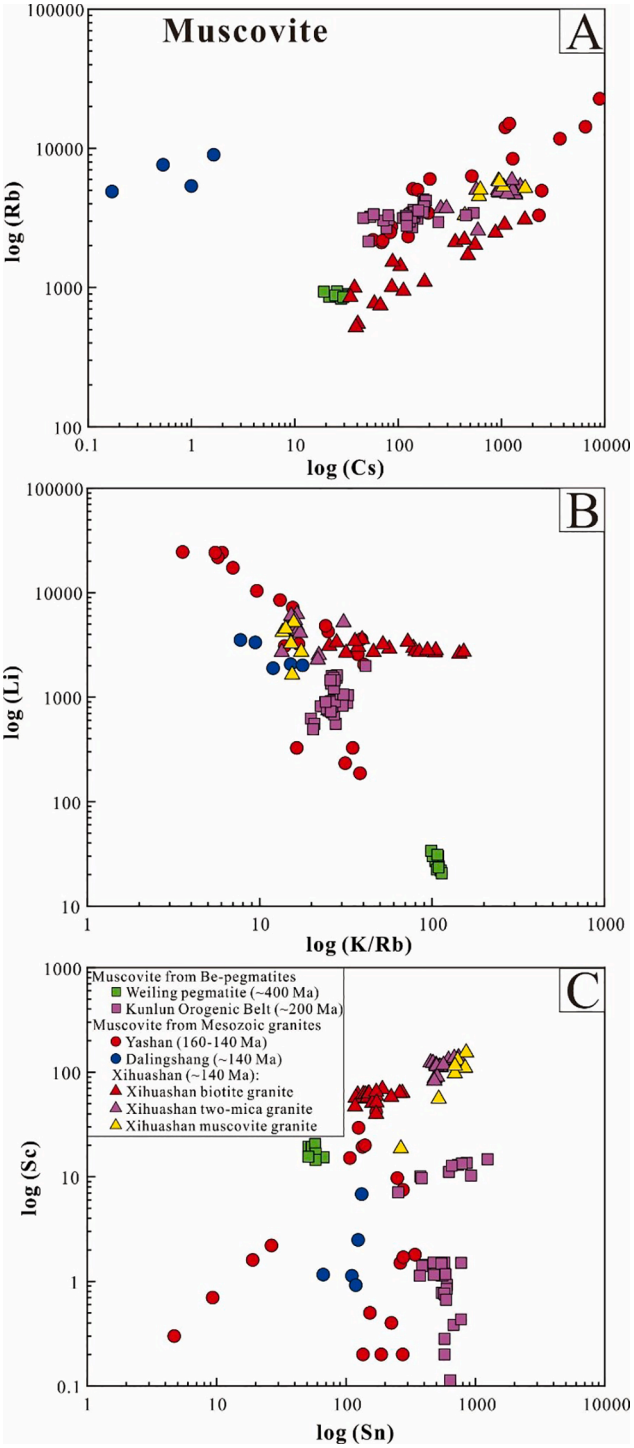

Fig. 6. Binary diagrams showing the trace element contents and ratios of muscovite from Be-pegmatites and granites. (A) log(Rb) vs. log(Cs); (B) log(Li) vs. log(K/Rb); (C) log(Sc) vs. log(Sn). Data sources: Be-pegmatites from the western Kunlun Orogenic Belt (Yan et al., 2022) and Weiling (Table 3), and granites from Yashan (Li et al., 2015), Dalingshang (Yin et al., 2019), and Xihuashan (Li et al., 2021).

(3) C-type inclusions: CO_2-bearing inclusions occur in both quartz and beryl. These three-phase inclusions ($V_{CO2} + L_{CO2} + L_{H2O}$) have 3–8 μm diameter and show a regular to irregular shape. This type of fluid inclusion accounts for 20 vol% of the total population. The carbonic phase accounts for 60–80 vol% of the total volume (Fig. 12A, C, D).

L-type, V-type, and C-type inclusions in quartz and beryl have CO_2 melting temperatures ranging from –58.1 to –55.1 ℃ and CO_2

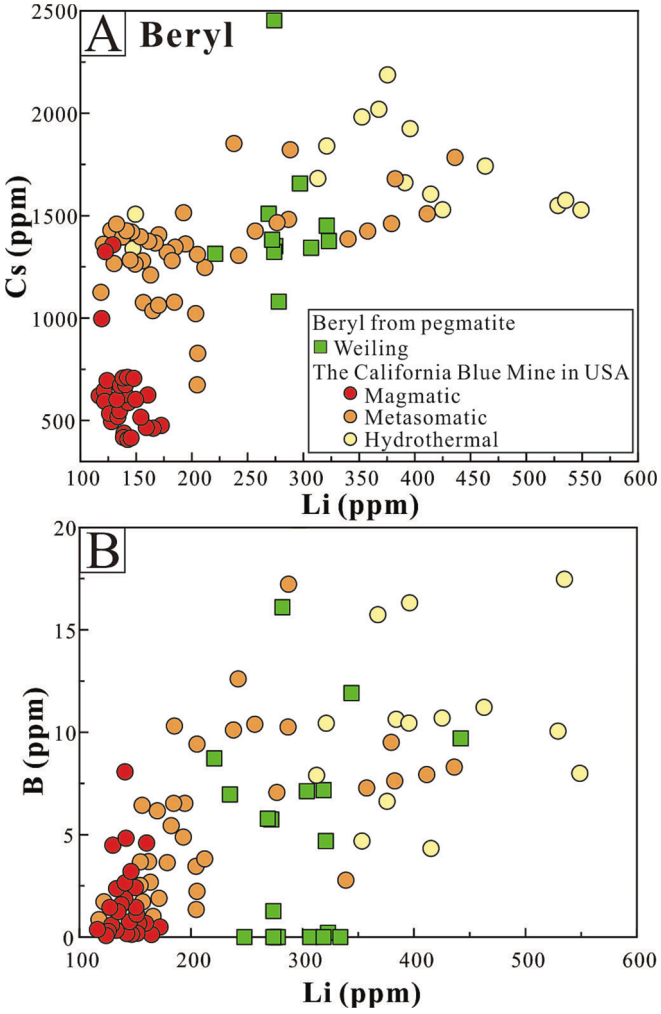

Fig. 7. Binary diagrams showing the trace element contents of beryl from the Weiling pegmatite. (A) Cs vs. Li; (B) B vs. Li. Data for the California Blue Mine topaz-beryl pegmatite (Pauly et al., 2021) are shown to highlight that the contents for Cs and Li increase systematically from magmatic to metasomatic and hydrothermal beryl. (For interpretation of the references to color in this figure legend, the reader is referred to the web version of this article.)

homogenization temperatures ranging from 25.2 to 27.8 ℃ (Fig. 13 and Table 10). Eutectic temperatures of –28.2 to –22.3 ℃ demonstrate the dominance of NaCl and KCl (Crawford 1981). The three types of inclusions homogenize at temperatures of 222–357 ℃ (Fig. 13A; Table 10). During heating, all L-type inclusions homogenize to the liquid phase and most V-type inclusions homogenize to the vapor phase. The final ice melting temperatures of L-type and V-type inclusions are –7.4 to –1.3 ℃, whereas clathrate melting temperatures of C-type inclusions range from 4.3 to 8.3 ℃. The salinities of fluid inclusions range from 3.3 to 10.9 wt% NaCl equiv (Fig. 13B) and the density of the fluid ranges from 0.62 to 0.86 g/cm^3. Raman spectroscopy demonstrates the presence of CO_2 in the vapor phase of L-type and C-type inclusions in quartz (Fig. 14A, B), H_2O in the liquid phase of L-type inclusions in quartz, and coexisting CO_2 and N_2 in the vapor phase of L-type inclusions in beryl (Fig. 14D).

5. Discussion

5.1. Age of the Weiling pegmatite

There were three major Phanerozoic phases of tectonic overprint in the SCB, i.e., an Early Paleozoic intracontinental orogeny with major

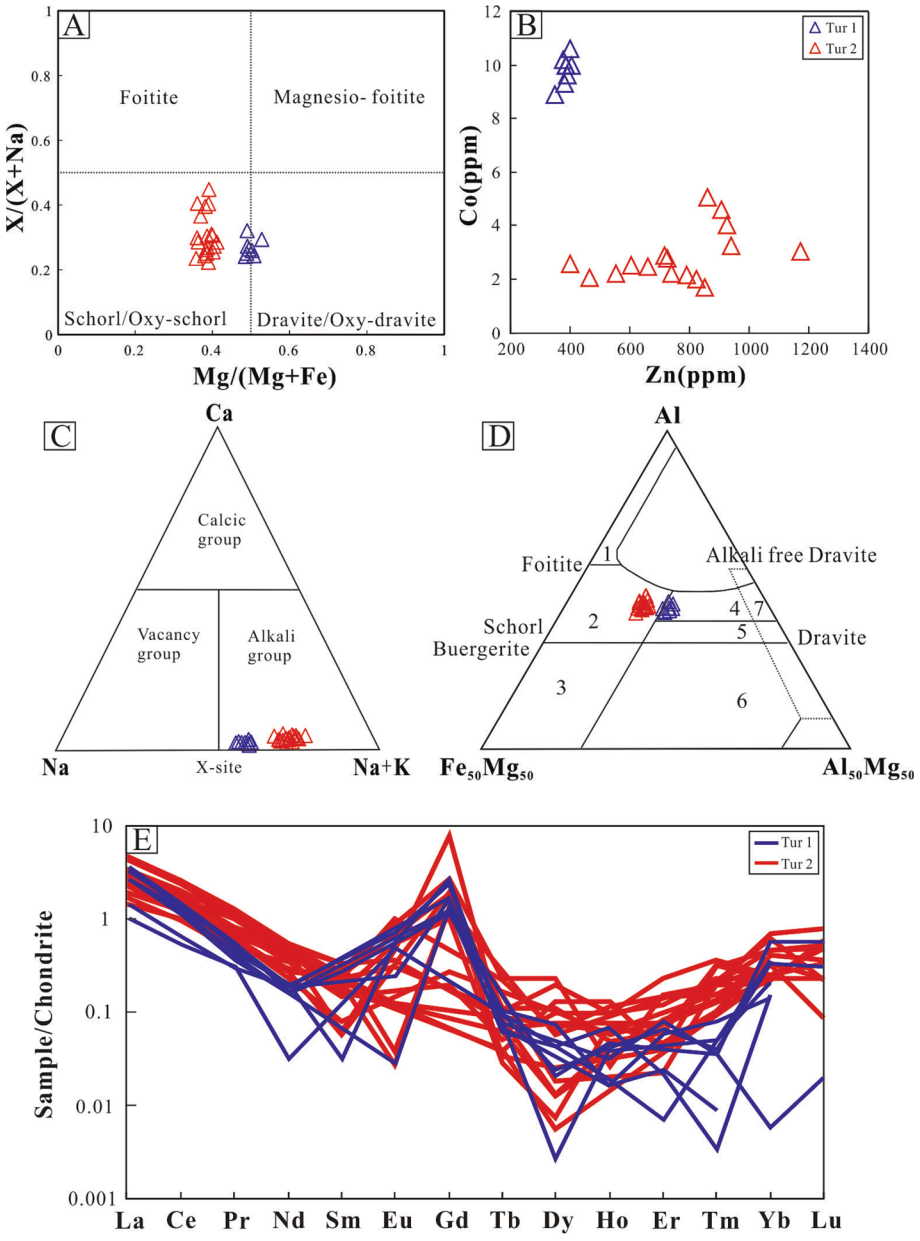

Fig. 8. Compositional variation of tourmaline from the Weiling pegmatite. (A) Tourmaline classification based on the calculated Mg/(Mg + Fe) versus X-site occupancy; (B) Co versus Zn; (C) Classification diagram of tourmaline from the Weiling pegmatite based on X-site occupancy (after Henry et al., 2011); (D) Ternary Al-Fe-Mg diagram showing composition of tourmaline from the Weiling pegmatite. The regions define the compositions of tourmaline from different rock types, according to Henry and Guidotti (1985). 1 = Li-rich granitoids and associated pegmatites and aplites; 2 = Li-poor granitoids and associated pegmatites and aplites; 3 = Fe^{3+}-rich quartz-tourmaline rocks (hydrothermally altered granites); 4 = Metapelites and metapsammites coexisting with an Al-saturating phase; 5 = Metapelites and metapsammites not coexisting with an Al-saturating phase; 6 = Fe^{3+}-rich quartz-tourmaline rocks, calc silicate rocks, and metapelites. (E) Chondrite normalized diagram of REE. Normalization values are after McDonough and Sun (1995).

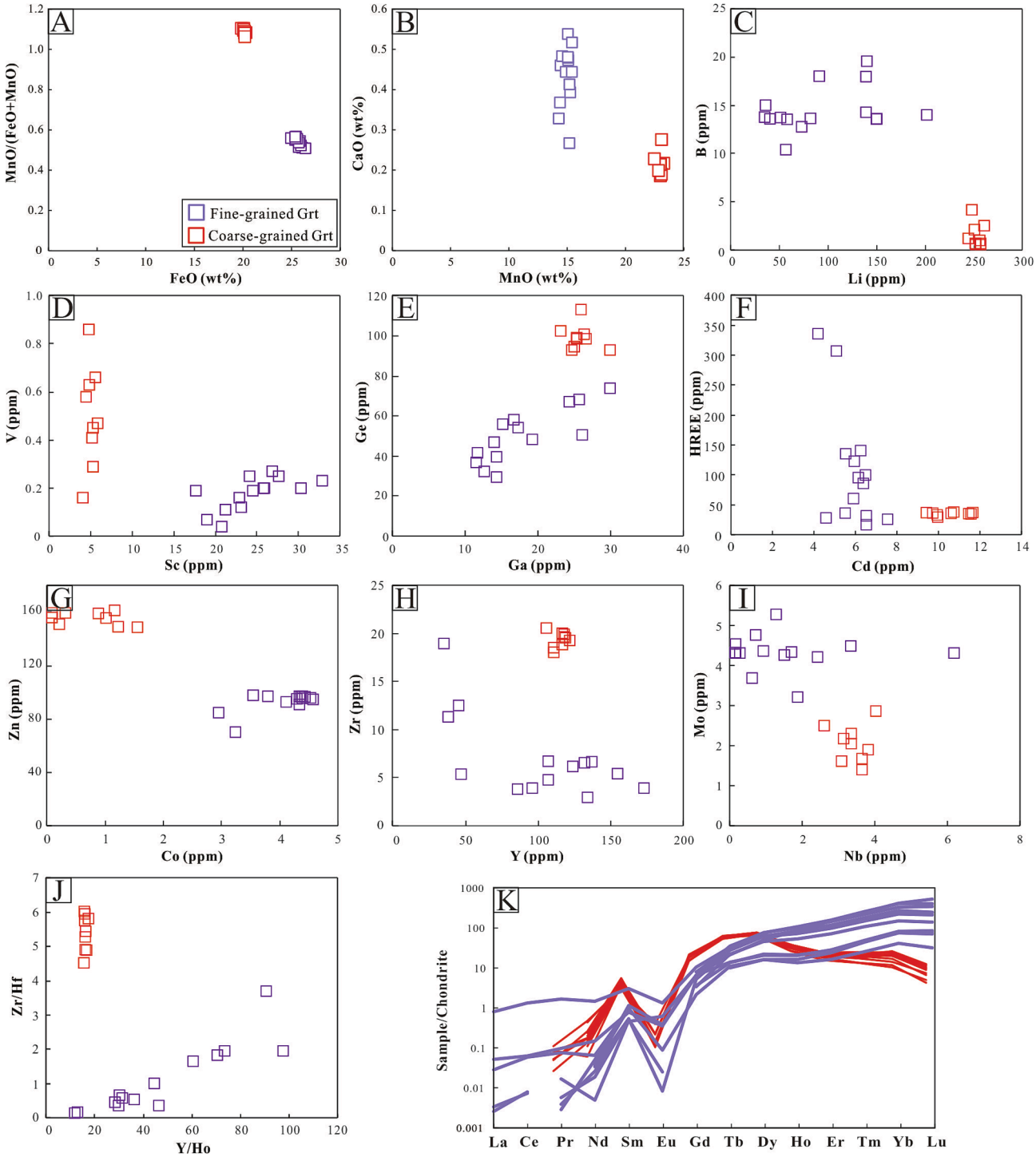

Fig. 9. Binary diagrams showing the major and trace element concentrations and ratios of garnet from the Weiling pegmatite. (A) MnO/(FeO + MnO) vs. FeO (wt. %); (B) CaO vs. MnO (wt.%); (C) B vs. Li (ppm); (D) V vs. Sc (ppm); (E) Ge vs. Ga (ppm); (F) HREE vs. Cd (ppm); (G) Zn vs. Co (ppm); (H) Zr vs. Y (ppm); (I) Mo vs. Nb (ppm); (J) Zr/Hf vs. Y/Ho; (K) Chondrite normalized diagram of REE. Normalization values are after McDonough and Sun (1995).

Table 8
LA-MC-ICP-MS boron isotopic analyses of tourmaline from the Weiling granitic pegmatite.

Analysis no.	Type	$\delta^{11}B$ (‰)	Analysis no.	Type	$\delta^{11}B$ (‰)	Analysis no.	Type	$\delta^{11}B$ (‰)
17WL-1–1	Tur 2	−11.9	15WL-21–1	Tur 2	−10.4	15WL-22–4	Tur 2	−10.8
17WL-1–2	Tur 2	−12.1	15WL-21–2	Tur 2	−10.1	15WL-22–5	Tur 2	−10.4
17WL-1–3	Tur 2	−12.0	15WL-21–3	Tur 2	−9.5	15WL-22–6	Tur 2	−10.7
17WL-1–4	Tur 2	−12.8	15WL-21–4	Tur 2	−9.6	15WL-22–7	Tur 2	−10.8
17WL-1–5	Tur 2	−12.6	15WL-21–5	Tur 2	−10.3	17WL-1–6	Tur 1	−12.4
15WL-17–1	Tur 2	−11.2	15WL-21–6	Tur 2	−10.1	15WL-17–8	Tur 1	−10.9
15WL-17–2	Tur 2	−11.9	15WL-21–7	Tur 2	−12.2	15WL-17–9	Tur 1	−11.7
15WL-17–3	Tur 2	−11.8	15WL-21–8	Tur 2	−11.0	15WL-21–9	Tur 1	−10.8
15WL-17–4	Tur 2	−11.8	15WL-22–1	Tur 2	−10.4	15WL-21–10	Tur 1	−10.9
15WL-17–5	Tur 2	−11.4	15WL-22–2	Tur 2	−10.2	15WL-22–8	Tur 1	−10.8
15WL-17–6	Tur 2	−11.6	15WL-22–3	Tur 2	−10.7	15WL-22–9	Tur 1	−11.1

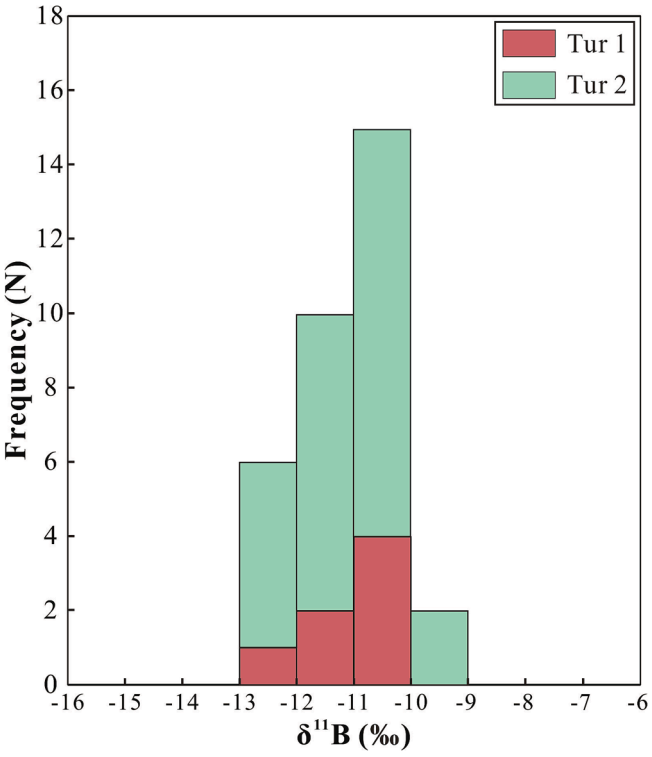

Fig. 10. Histogram of boron isotopic composition of tourmaline.

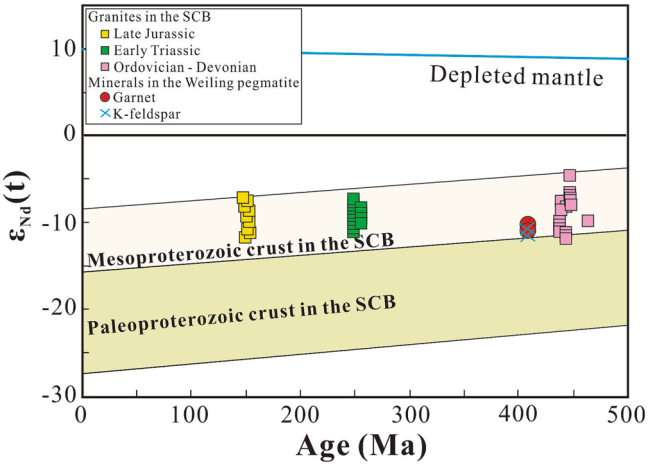

Fig. 11. Evolution diagram for the Nd isotopic composition of differently-aged crust in the South China Block. The Nd isotopic composition of pegmatitic minerals from the Weiling pegmatite (garnet and feldspar) falls on the same Nd evolution trend as Jurassic, Triassic, and Paleozoic granites from the South China Block. The Nd isotope ranges of Proterozoic metasedimentary rocks in the SCB are from Chen and Jahn (1998). Data source: Early Paleozoic granites (Wang et al., 2011b; Shu et al., 2015); Early Triassic granites (Wang et al., 2007b; Shu et al., 2015); Late Jurassic granites (Liu et al., 2021).

crustal thickening, the Triassic collision between the Indochina Block and the SCB in response to the closure of the Paleo-Tethys Ocean, and the Jurassic-Cretaceous subduction of the Paleo-Pacific plate (Song et al., 2015; Wang et al., 2007a; Wang et al., 2011). Major granite-related polymetallic mineralization is associated with highly-fractionated S-type granites that formed during these tectonic events. Jurassic and Cretaceous Sn and W mineralization is economically most important (Jiang et al., 2020). Based on field occurrence alone, the Weiling beryl-bearing pegmatite could be related to any of these magmatic and metamorphic events.

The dated muscovite has slightly low K_2O contents (Table 3), which indicates that the muscovite might have been slightly altered. Therefore, it is a priori not clear whether the plateau age of 405.33 ± 3.38 Ma really dates a Paleozoic event or is too old because of the alteration with possible additions of excess argon. To resolve this ambiguity, mineral separates of garnet from the concentric structures were dated using the U-Pb method. The U contents of garnet are low and the Pb isotopic compositions are not very radiogenic. Therefore, the garnet U-Pb age is not very precise. The U-Pb data, however, clearly show that the Weiling pegmatite formed during an Early Paleozoic tectonic event affecting the SCB. This finding agrees broadly with the zircon U-Pb isochron age of 388.5 ± 3.1 Ma reported by Zheng et al. (2023). The age data demonstrate that the Weiling beryl-bearing pegmatite is not related to the Jurassic-Cretaceous magmatism that accounts for Sn and W

Table 9
Nd isotopic analyses of garnet and feldspar from the Weiling granitic pegmatite.

Sample	Mineral	Age (Ma)	Sm (ppm) [a]	Nd (ppm) [a]	$^{147}Sm/^{144}Nd$ [b]	$^{143}Nd/^{144}Nd \pm 2\sigma$ [b]	ε_{Nd} (t = 407 Ma) [c]
15WL-14-Grt	Garnet	407	0.83	2.45	0.2044	0.512056 ± 4	−11.35
15WL-16-Grt	Garnet	407	1.47	4.25	0.2093	0.512021 ± 4	−12.03
15WL-14-fsp	Feldspar	407	0.09	0.31	0.1737	0.511984 ± 6	−12.76
15WL-16-fsp	Feldspar	407	0.29	0.97	0.1778	0.511972 ± 3	−12.98

[a] Measured concentration of isotopes in garnet and feldspar.
[b] Measured isotopic ratios in garnet and feldspar.
[c] Calculated using $(^{143}Nd/^{144}Nd)^0_{CHUR} = 0.512638$ and emplacement age of 407 Ma.

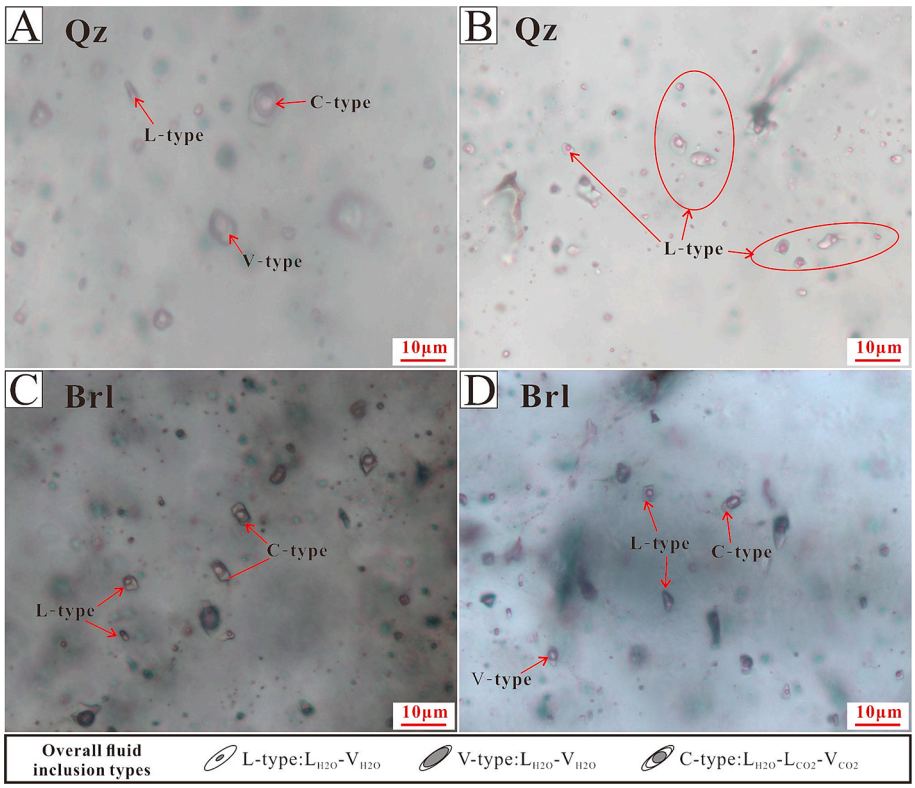

Fig. 12. Sketch and photomicrographs showing types and distribution of fluid inclusions in quartz and beryl from the Weiling pegmatite. Qz = Quartz; Brl = Beryl.

mineralization in the SCB, although most of Be mineralization in the SCB is related to Jurassic and Cretaceous Sn and W mineralization. The age data cannot distinguish whether the Weiling pegmatite is related to the Early Paleozoic high-grade metamorphism affecting the area (Zhang et al., 2009) or to post-orogenic Paleozoic intrusions.

5.2. Source and mobilization of pegmatitic melt

The Weiling pegmatite contains abundant tourmaline, beryl, garnet, and muscovite, all of which are typical for granitic rocks originating from the partial melting of sedimentary rocks. Pegmatites with this mineral assemblage typically are classified as LCT-type pegmatites that apart from enrichment of B and P also may have enhanced contents of rare metals and/or Be (Cerny and Ercit, 2005).

The $\delta^{11}B$ values of tourmaline from the Weiling pegmatite (-12.8 ‰ to −9.5 ‰) are similar to those of the continental crust (Palmer and Slack, 1989; Marschall and Jiang, 2011), suggesting a continental crustal origin (Fig. 10). Pegmatitic minerals – feldspar and garnet – from the Weiling pegmatite have ε_{Nd} (t) values of −12.98 to −11.35 (Fig. 11). These values are similar to those of Early Paleozoic granites from the SCB (-14.9 ~ -11.7, Liu et al., 2021) and fall into the compositional evolution trend of Paleo-Meso Proterozoic basement rocks (Fig. 11). Thus, both the Weiling pegmatite and the Early Paleozoic granites are likely to have been generated by partial melting of metasedimentary rocks without significant input of mantle material (Song et al., 2015; Fig. 11). Furthermore, the similar ε_{Nd} (t) values suggest that regional Early Paleozoic granites (if present at depth) could be parental rocks of the Weiling pegmatite.

Although the nature of accessory and ore minerals and the isotopic compositions of Nd and B clearly indicate sedimentary protoliths for the pegmatitic melts, it is a priori not clear whether the Weiling pegmatite is linked to a S-type granite or represents local anatectic melts. In the first case, the pegmatitic melts are the result of extensive magmatic fractionation and the pegmatite should be spatially and genetically related to a nearby coeval granite. On the local scale, there are no outcrops of intrusions of appropriately chemical composition and age (Fig. 1C), although it may be argued that such intrusions could be present at depth. In the second case, the pegmatites are related to the metamorphism and migmatization of regional sedimentary rocks of the Zhoutan Formation induced by decompression and head advection by the emplacement of high-grade metamorphic nappes or the emplacement of melts from the lower crust or the mantle. Both processes of pegmatite formation yield similar $\delta^{11}B$, and ε_{Nd}(t) values with regional early Paleozoic granites.

5.3. The Weiling pegmatite: A highly fractionated melt or a small-volume partial melt

The chemical composition of pegmatitic melt reflects the source rocks and internal fractionation processes, which are particularly important in zoned pegmatites (Trumbull et al., 2013; Morgan and London, 1989). For pegmatites that are derived from a parent granite, the chemical composition of the pegmatite is also affected by the early magmatic fractionation of the parent granitic melt. Because of the large crystal size of pegmatites, it is generally difficult to get representative bulk rock samples. Therefore, the composition of pegmatitic minerals is commonly used to monitor the composition of the melts/fluids forming the pegmatite (Morgan and London, 1989).

The chemical compositions of pegmatitic minerals differ between anatectic melts and highly fractionated residual melts (Michallik et al., 2017; Tian et al., 2020; Jiang et al., 2021; Luo et al., 2022). We use this dependence of mineral chemistry on the mode of pegmatite formation to address the petrogenesis of the Weiling pegmatite by comparing trace element signatures of muscovite, K-feldspar, tourmaline, and beryl from the Weiling pegmatite with the corresponding signatures of minerals from pegmatites of unequivocal genesis, i.e., highly fractionated pegmatites or anatectic pegmatites.

Muscovite from the Weiling pegmatite has low contents and relatively narrow ranges of Rb, Cs, Li, Sc, and Sn, and high K/Rb ratios (Fig. 6), which is in contrast to muscovite from highly fractionated melts, such as the Mesozoic highly fractionated muscovite granites in

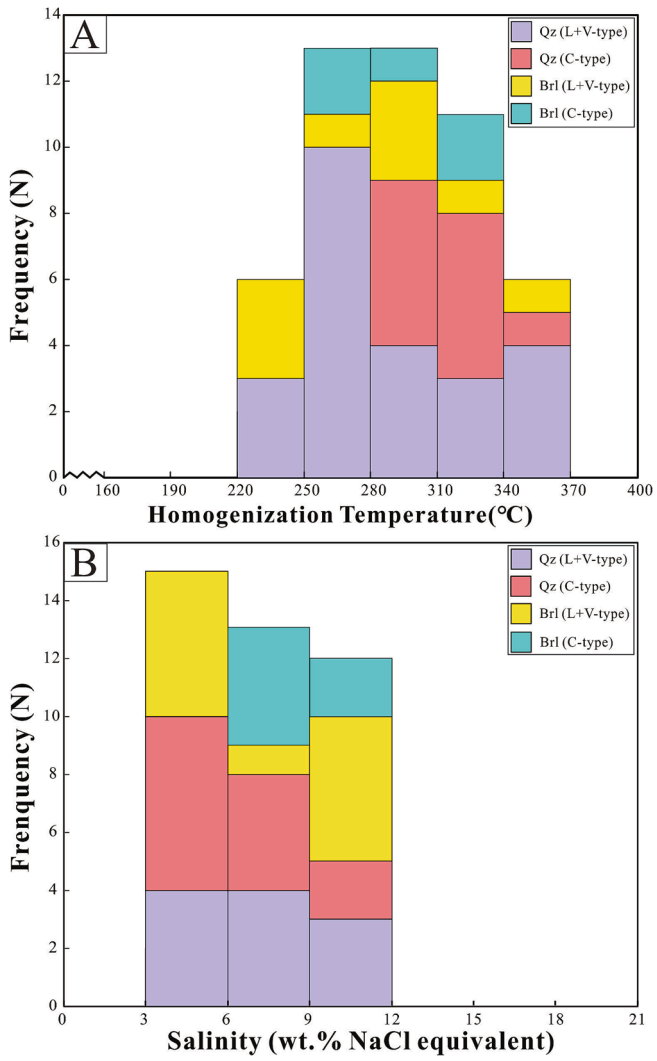

Fig. 13. Histograms of homogenization temperatures and salinities of fluid inclusions in quartz and beryl from the Weiling pegmatite.

Yashan, Dalingshang, and Xihuashan granites, the Be-pegmatites along the western Kunlun Orogenic Belt that formed by fractional crystallization (Fig. 6). Muscovite from the Be-pegmatites along the western Kunlun Orogenic Belt formed by fractional crystallization and has similar compositions as muscovite from the Mesozoic granites of the SCB with W-Sn-Be-Nb-Ta deposits. Muscovite from magmatic systems has much higher contents and variations of these elements (Rb, Cs, Li, Sc, and Sn) and lower K/Rb ratios (Fig. 6). The high trace element contents reflect two features, availability of the trace elements in the source and incompatible behavior during melt evolution. For instance, the correlated increase of Sn and Sc in muscovite from differently evolved types of the Xihuashan granite (Fig. 6C) shows that both elements were available in the granite source and behaved incompatible during magma evolution. Low contents of the incompatible trace elements Li, Rb, and Cs indicate that the melt did not experience significant fractionation. Muscovite from little-evolved Xihuashan biotite granite shows low Cs and Rb contents, and high ratio of K/Rb, similar to muscovite from the Weiling pegmatite. Therefore, the low contents of Rb, Cs, Li, Sc, and Sn in muscovite from the Weiling pegmatite demonstrate that this pegmatite crystallized from a little-evolved melt. This conclusion is also supported by the low Rb (458–533 ppm) and Cs (20.4–54.5 ppm) contents and the high K/Rb ratios (238–296) of K-feldspar from the Weiling pegmatite (Table 7) that differ markedly from the values known from highly evolved beryl-enriched granites, i.e., Rb > 3000 ppm, Cs > 100 ppm, and K/Rb < 30 (Selway et al., 2005), the pegmatitic leucogranites with K/Rb varying from 24 to 132 (Černý et al., 2005), and the barren pegmatites with K/Rb varying from 158 to 216 (Hulsbosch et al., 2014). These ranges preclude the possibility that the Weiling pegmatite is the result of fractional crystallization.

The composition of pegmatitic minerals is used to estimate the degree of fraction (Morgan and London, 1989). For instance, the chemical composition of tourmaline in complex zoned pegmatites varies with fractionation from schorl-dravite in the little evolved border and wall zones to varicolored elbaite in the highly evolved inner zones (Trumbull et al., 2013). Tourmaline from the Weiling pegmatite belongs to the schorl-dravite series (Fig. 8A), indicating the Weiling pegmatite experienced only a low degree of fractionation, in line with the low contents of Rb (831–932 ppm), Cs (19.1–32.3 ppm), and Li (22.4–33.8 ppm) in muscovite (Fig. 6A, B), and the low contents of Rb (458–533 ppm) and Cs (20.4–54.5 ppm) and high K/Rb ratio (238–296) in K-feldspar. Both tourmaline and garnet from different mineral assemblage have variations of Fe and Mg contents (Fig. 8A, 9A), which could represent a reservoir effect, i.e., as early crystallized minerals extracted mainly Fe, later grown minerals had higher Mg contents. The trace and rare earth elements in tourmaline and garnet from different mineral assemblages vary significantly (Figs. 8 and 9), which could reflect non-homogenized melts that are derived from the partial melting of heterogeneous metasedimentary source rocks or different degrees of partial melting from a homogeneous source. The B concentrations of beryl are low and highly variable (Fig. 7).

Magmatic, metasomatic, and hydrothermal beryl from the California Blue pegmatite has contrasting trace element contents (Pauly et al., 2021). Primary magmatic beryl has low concentrations of Cs < 700 ppm, Li < 200 ppm, and B < 5 ppm, whereas metasomatic and hydrothermal beryl seems to have markedly higher and heterogeneous contents of these elements (Pauly et al., 2021). Beryl from the Weiling pegmatite has high and variable contents of Li, B, and Cs, similar to metasomatic and hydrothermal beryl from the Bule Mine pegmatite (Fig. 7). A hydrothermal origin of beryl is in line with the abundance of fractures and fluid inclusions (Fig. 4D, Fig. 12C, D) and the low homogenization temperatures of fluid inclusions (Fig. 13A). As there seems to be no primary magmatic beryl in the Weiling pegmatite, its composition does not reflect the evolution history of the pegmatitic melt.

Granites that may form rare-metal pegmatites commonly are peraluminous to strongly peraluminous and highly-evolved. Typically, fertile granite and pegmatitic leucogranite have low ratios of K/Rb < 100, Ba/Rb < 1.8, Mg/Li < 10, and Nb/Ta < 8 (Selway et al., 2005; Černý et al., 2005; Ballouard et al., 2016; Lv et al., 2021). Early Paleozoic granites around the NWA, e.g., Yihuang and Fufang granites, as well as typical Early Paleozoic granites of the SCB show high ratios of K/Rb > 100, Ba/Rb > 1.8, Mg/Li > 10, and Nb/Ta > 8 (Fig. 16), indicating that these granites are weakly differentiated and, therefore, unlikely to be precursors of beryl-bearing pegmatites. Furthermore, the Early Paleozoic granites in the SCB have low Be contents (3.4–3.5 ppm, Liu 1975) and do not represent an adequate Be source for the Weiling pegmatite. For comparison, granites with beryllium deposits typically have Be contents of 10–27 ppm (Liu 1975). Thus, the absence of favorable fertile granites for Be-pegmatites supports the conclusion – obtained from the chemical compositions of muscovite and K-feldspar – that the Weiling pegmatite evolved from an anatectic melt. Mesozoic granites of the SCB having relatively high Be contents (15.7–33.7 ppm, Liu 1975), are highly fractionated and may have associated W ± Sn mineralization. Typically, Mesozoic Be mineralization is associated with those W-Sn deposits. Mesozoic Be-pegmatites in the SCB are linked to highly evolved granites (Tian et al., 2020; Wen et al., 2021). Even though it is quite likely that Paleozoic and Mesozoic granites involved the same source rocks (Fig. 11), the contrasting metal endowment of the two groups of granites indicates that they formed at different melting temperatures (e.g., Yuan et al., 2019), with generally insignificant mobilization of Be, Sn and W during Paleozoic melting and significant mobilization of these metals, in particular Sn and W during Mesozoic melting.

Table 10
Summary of the microthermometric data of fluid inclusions trapped in quartz and beryl from the Weiling granitic pegmatite.

Group	Host Mineral	FIs type	Number	Tm-co_2 (℃)	Tm-eu (℃)	Tm-ice (℃)	Tm-cla (℃)	Th-co_2 (℃)	Th (℃)	Salinity (wt.% NaCl equivalent)	Density (g/cm^3)
Group01	Quartz	L + V-type	2		−22.3	−3.9			285	6.3	0.79
Group02	Quartz	L + V-type	4		−25.8	−3.6			258	5.9	0.83
Group03	Quartz	L + V-type	3		−25.3	−4.6			354	7.3	0.75
Group04	Quartz	L + V-type	3						338		0.62
Group05	Quartz	L + V + C-type	4			−6.7	4.3		260	10.1 10.0	0.78
Group06	Quartz	L + V + C-type	3	−57.1		−4.7	6.5	26.4	253	7.5 6.5	0.85
Group07	Quartz	C-type	2	−55.1			5.2	26.4	357	8.7	0.57
Group08	Quartz	C-type	3	−57.8			8.3	26.9	302	3.3	0.70
Group09	Quartz	L + V + C-type	4		−28.2	−2.2	7.5	27.8	302	3.7 4.9	0.70
Group10	Quartz	L + V + C-type	3			−4.9	5.6	25.2	253	7.7 8.0	0.79
Group11	Quartz	L + V-type	2		−22.3				267	5.7	0.76
Group12	Quartz	L + V-type	1						255		0.78
Group13	Quartz	L + V-type	1		−25.3				296		0.79
Group14	Quartz	L + V-type	2			−2.2			245	3.7	0.80
Group15	Quartz	L + V-type	1		−26.7				295		0.75
Group16	Beryl	L + V-type	2		−23.2	−3.1			347	5.1	0.71
Group17	Beryl	L + V-type	4		−24.5	−4.1			222	6.6	0.78
Group18	Beryl	L + V-type	1		−22.6				225		0.83
Group19	Beryl	L + V-type	2			−2.3			267	3.9	0.82
Group20	Beryl	L + V-type	1			−2.3			235	3.9	0.82
Group21	Beryl	L + V-type	3		−26.5	−2.1			295	3.6	0.71
Group22	Beryl	L + V-type	2		−22.4	−2.0			281	3.4	0.74
Group23	Beryl	L + V-type	3		−26.5	−7.4			300	11.0	0.70
Group24	Beryl	C-type	2	−58.1			7.5		275	6.8	0.86
Group25	Beryl	L + V + C-type	3			−7.3	4.3		315	10.0 10.9	0.73

Abbreviation: $T_{m\text{-}CO2}$: melting temperature of solid CO_2; T_{eu}: eutectic temperature of aqueous fluid inclusions; $T_{m\text{-}cla}$: melting temperature of the clathrate; $T_{h\text{-}CO2}$: homogenization temperature of CO_2; $T_{m\text{-}ice}$: final ice-melting temperature; T_h: total homogenization temperature.

5.4. Role of fluids and post-crystallization alteration

Many beryl-bearing rare-metal deposits in the Altai Pegmatite District, the Western Kunlun Orogenic Belt, and the Songpan-Ganzi Pegmatite Belt of western China formed from medium-temperature, low-salinity, high-density and CO_2-rich fluids (Fig. 15; Liu et al., 2012; Ashworth 2014; Qin 2014; Ding and Li, 2015; Xiong et al., 2015; Huang et al., 2017; Mulja and Williams-Jones, 2018; Hu 2019). The CO_2-rich ore-forming fluids are commonly present in LCT pegmatites, e.g., Jiajika (Yang et al, 2020) and Lijiagou (Fei et al., 2021) in the Songpan-Ganzi Pegmatite Belt. In some pegmatites the fluid has minor CH_4 and N_2, e.g., the beryl mineralization of the Cuonadong gneiss dome in southern Tibet of China (Hu 2019) and the Tanco Li-Be-pegmatite in Canada (London 1986). For the studied Weiling pegmatite, the ore-forming fluid contained also CO_2 and N_2 (Fig. 14). Fluxing components (CO_2, N_2, F, P, and B) could decrease the viscosity of melts/fluids and the solidus temperature of granitic melts, thereby allow for higher differentiation and higher concentrations of rare metals (Raimbault et al., 1995). In contrast, high-viscosity melts in the super-cooling environment, which could be caused by high contents of Be, always show characteristic graphic textures. For example, the Be-pegmatites of the Weiling in the SCB, as well as Altay Pegmatite District (e.g., Azubai and Jiamukai) have well developed graphic textures. Therefore, the presence of graphic structure of pegmatite is used as a guide in prospection of Be-pegmatites.

Quartz and beryl have L-type, V-type and C-type fluid inclusions that occur together (Fig. 12A, D), which means the simultaneous presence of aqueous-carbonic and aqueous fluids. Quartz and beryl have similar homogenization temperatures and salinities for L-type, V-type and C-type inclusions (Figs. 13 and 15). Fluid inclusions from the Weiling pegmatite yield much lower temperatures than the melting temperature of most granitic pegmatites (420–650 ℃), even for P-rich and B-rich systems (Li et al., 2017). Instead, homogenization temperatures of fluid inclusion are similar to those from many Li-Be-pegmatites (Fig. 15) such as the Jiajika Li-rich granitic pegmatite (250–350 ℃) (Yang et al., 2020), and the main emerald mineralization stage of the Dayakou emerald deposit (300–360 ℃) (Long et al., 2021). One possible explanation for medium–low homogenization temperatures of the ore-forming fluid is that beryl formed during the late hydrothermal stage of the Weiling pegmatite. This interpretation, however, does not explain the medium homogenization temperatures and low salinities of fluid inclusions in quartz. Alternatively, the fluid inclusions could reflect secondary hydrothermal processes related to the exsolution of late fluids from the pegmatite melt. Such a late separation of a magmatic fluid with separation into aqueous and CO_2 phases also explains the heterogeneous entrapment in quartz and beryl at temperatures between 222 and 357 ℃.

5.5. The tectonic setting of the Weiling pegmatite

The SCB hosts numerous rare-metal deposits, in particular of Sn, W, and Be (Fig. 1A) that formed in different tectonic settings and at different time (Jingwen et al., 2013, 2019). For instance, the W-Mo deposits are related to oxidized granites that received major input from the lithospheric mantle and formed in extensional settings (Jingwen et al., 2013). In contrast, Sn-W and Be deposits are mainly related to reduced granites. Although Sn, W, and Be mineralization in the SCB may involve the same protoliths, intensity of mineralization varies significantly with time. The most important mineralization in the SCB is related to Jurassic and Cretaceous granites, and there is also significant Triassic mineralization. In contrast, Paleozoic granites and pegmatites only have minor mineralization, i.e., Be in some pegmatites and Mo in the Wuyi-Yunkai Domain farther to the southwest. This temporal variation seems to be related to the processes that mobilize these metals from the protoliths into the melt, in particular in dependence of melting temperatures and the mineral assemblages of the restites (Wolf et al., 2018). The mobilization of Sn seems to be controlled by biotite-

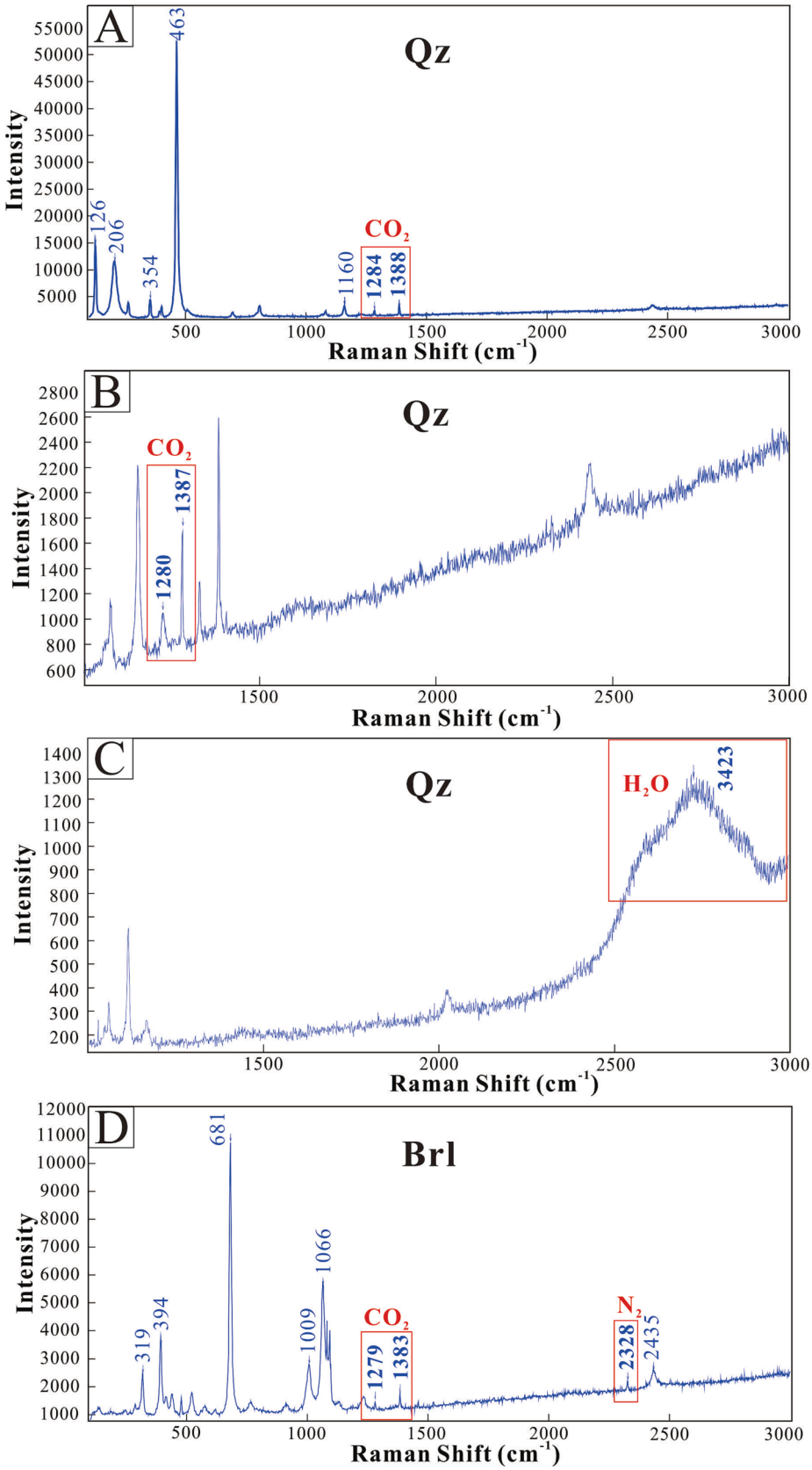

Fig. 14. Representative laser Raman spectra for fluid inclusions from the Weiling pegmatite. (A) CO_2 spectra of the vapor phase in L-type inclusion of quartz; (B) CO_2 spectra of the vapor phase in C-type inclusion of quartz; (C) H_2O spectra of the liquid phase in L-type inclusion of quartz; (D) CO_2 and N_2 spectra of the vapor phase in L-type inclusion of beryl. Qz = Quartz; Brl = Beryl.

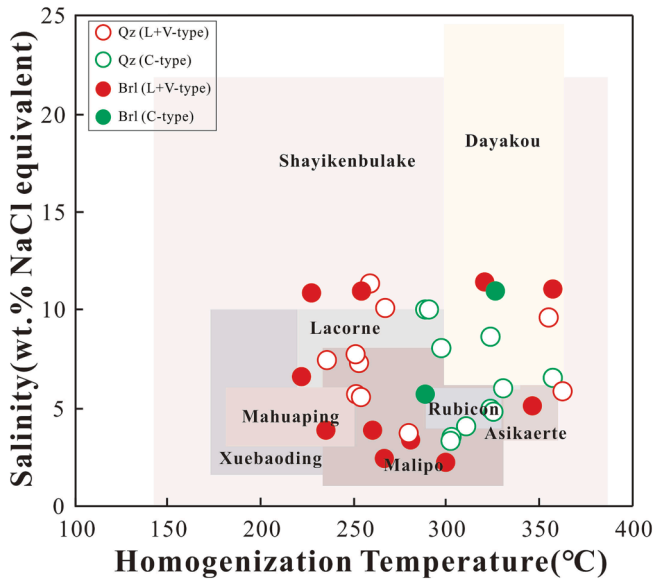

Fig. 15. Comparison for temperature and salinity of fluid inclusions in the Weiling pegmatite and other beryl-bearing beryllium deposits worldwide. Data for other beryl-bearing deposits from Liu et al. (2012), Ashworth (2014), Qin (2014), Xiong et al. (2015), Ding and Li (2015), Huang et al. (2017), Mulja and Williams-Jones (2018), and Long et al. (2021). Qz = Quartz; Brl = Beryl.

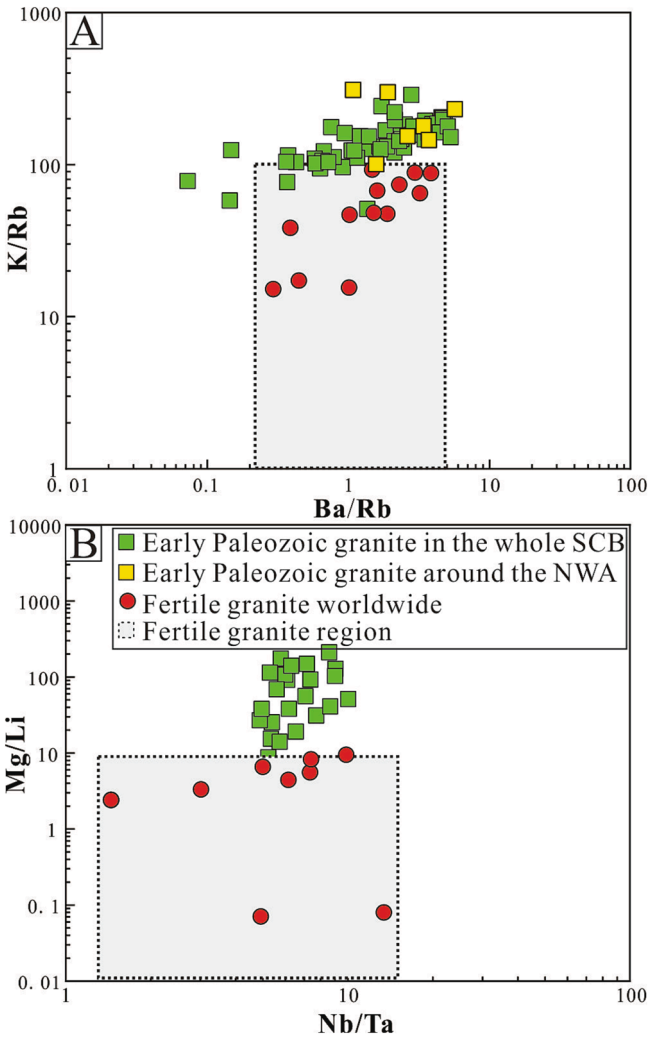

Fig. 16. Diagrams of K/Rb vs. Ba/Rb (A), and Mg/Li vs. Nb/Ta (B) of the Early Paleozoic granites from the SCB and typical fertile granite worldwide, showing the low differentiation degree of the former. Data sources: Early Paleozoic granites of South China Block from Bai et al. (2006, 2014, 2015); Li et al. (2006); Tian et al. (2020); and He et al. (2022); Field for fertile granites according to Selway et al. (2005), Zou and Li (2006) and Cerny et al. (2012).

dehydration melting, which occurs at higher temperature than muscovite-dehydration melting. Furthermore, the loss of low-temperature partial melts seems to be essential for the enrichment of Sn in high-temperature partial melts (Wolf et al., 2018). In contrast, W and Be are mainly mobilized already at lower temperature during muscovite-dehydration melting (Yuan et al., 2019). These constraints may explain why Sn mineralization is rare in Paleozoic granites of the SBC and Be occurs both (i) in Paleozoic and Mesozoic pegmatites with no or only subordinate W or Sn and (ii) in Mesozoic late-magmatic vein-type mineralization associated with W. The Be-rich melts may be generated by partial melting of metasedimentary rocks by (i) muscovite dehydration melting if Be released from decomposed muscovite is not sequestered in stable restite phases and by (ii) influx of CO_2-rich fluids that trigger dehydration melting (Cuney and Barbey 2014). The Weiling pegmatite possibly is derived from the partial melting of Zhoutan Formation metapelites under amphibolite facies conditions or by fluid input along regional shear zones.

Early Paleozoic granitoids in the SCB fall into two age groups. The older age group includes 460–435 Ma *syn*-orogenic granites related to the intracontinental high-grade metamorphism. The younger group, which is far more voluminous, includes 435–400 Ma granites that post-date the metamorphic peak and that were emplaced in a setting of extension (Zhang et al., 2009; Chen et al., 2018). The Weiling super-large granitic pegmatite falls in the younger age group when an extensional setting prevailed. Such a setting is in line with the observation that most large-scale rare metal pegmatites in the world form in late and post-orogenic settings (Černý 1991; Yan et al., 2022), i.e., postdate the peak of regional metamorphism (Lv et al., 2018).

6. Conclusions

(1) The Weiling granitic pegmatite possibly formed at ca. 405 Ma. The pegmatite shows a low degree of fractionation. The B isotopic compositions of tourmaline and the Nd isotopic compositions of K-feldspar and garnet of the pegmatite indicate that the melts were derived from crustal sources without input of mantle component.

(2) The mineral assemblage, mineral chemistry, and B and Nd isotopic compositions indicate that the Weiling granitic pegmatite is a LCT pegmatite that resulted from low pressure muscovite melting of metasedimentary rocks of the Zhoutan Formation. These sedimentary rocks were likely the source of Be.

(3) The Weiling beryl mineralization formed in the medium-temperature, low-salinity and high-density, B-rich, Li-poor H_2O-NaCl-KCl-CO_2-N_2 system.

Declaration of Competing Interest

The authors declare that they have no known competing financial interests or personal relationships that could have appeared to influence the work reported in this paper.

Data availability

All data are in the paper.

Acknowledgments

This research was funded by the National Natural Science Foundation of China (no. 92162323) and the special fund from the State Key Laboratory of Geological Processes and Mineral Resources, China University of Geosciences (no. MSFGPMR03-2) awarded to Shao-Yong Jiang and a grant from the China Scholarship Council (grant no. 202006410082) awarded to Xiu-Fang Lei. We thank the editor and two reviewers who provided valuable comments that improved significantly the paper

References

Ashworth, L., 2014. Mineralized pegmatites of the Damara Belt, Namibia: Fluid inclusion and geochemical characteristics with implications for post-collisional mineralization. University of the Witwatersrand. PhD thesis.

Bai, D.Y., Huang, J.Z., Ma, T.Q., Wang, X.H., 2006. Geology and geochemistry of the Silurian Penggongmiao granitic pluton in the southeastern Hunan Province and its implication for tectonic setting. Geoscience 20, 130–140.

Bai, D.Y., Zhong, X., Jia, P.Y., Xiong, X., Huang, W.Y., 2014. Zircon SHRIMP U-Pb dating and geochemistry of Caledonian Miao'ershan pluton in the western part of the Nanling Mountains and their tectonic significance. Acta Petrol. Miner. 33, 407–423 in Chinese with English abstract.

Bai, D.Y., Zhong, X., Jia, P.Y., Xiong, X., Huang, W.Y., 2015. Zircon SHRIMP U-Pb dating, geochemical characteristics and tectonic setting of Caledonian Yuechengling pluton in the western segment of the Nanling mountains. Geochimica 44, 27–42.

Ballouard, C., Poujol, M., Boulvais, P., Branquet, Y., Tartèse, R., Vigneresse, J.-L., 2016. Nb-Ta fractionation in peraluminous granites: a marker of the magmatic-hydrothermal transition. Geology 44 (3), 231–234.

BGMEDJP., 2017. (Bureau of geology and mineral exploration and development of Jiangxi Province). The topographic map and line-3 geological profile map of the Weiling pegmatite, Jiangxi Province. Unpublished map in China.

Bodnar, R.J., Vityk, M.O., 1994. Interpretation of microthermometric data for H_2O-NaCl fluid inclusions. In: De Vivo, B., Frezzotti, M.L. (Eds.), Fluid inclusions in Minerals, Methods and Applications. Virginia Tech, Blacksburg, pp. 117–130.

Černý, P., 1991. Rare-element granitic pegmatites. II. Regional to global environments and petrogenesis. Geosci. Canada. 18, 68–81.

Cerny, P., Ercit, T.S., 2005. The classification of granitic pegmatites revisited. Can. Mineral. 43 (6), 2005–2026.

Cerny, P., Halden, N.M., Ferreira, K., Meintzer, R.E., Brisbin, W.C., Chackowsky, L.E., Corkery, M.T., Longstaffe, F.J., Trueman, D.L., 2012. Extreme fractionation and deformation of the leucogranite-pegmatite suite at Red Cross lake, Manitoba, Canada. II. Petrology of the leucogranites and pegmatites. Can. Mineral. 50 (6), 1807–1822.

Černý, P., Masau, M., Goad, B.E., Ferreira, K., 2005. The Greer Lake leucogranite, Manitoba, and the origin of lepidolite-subtype granitic pegmatites. Lithos 80 (1-4), 305–321.

Che, X.D., Wang, R.C., Wu, F.Y., Zhu, Z.Y., Zhang, W.L., Hu, H., Xie, L., Liu, J.J., Zhang, D., 2019. Episodic Nb-Ta mineralization in South China: constraints from in situ LA-ICP-MS columbite-tantalite U-Pb dating. Ore Geol. Rev. 105, 71–85.

Chen, J., Jahn, B.-M., 1998. Crustal evolution of southeastern China: Nd and Sr isotopic evidence. Tectonophysics 284 (1-2), 101–133.

Chen, X.L., Liang, H.Y., Richards, J.P., Huang, W.T., Zhang, J., Wu, J., Sotiriou, P., 2018. Age and granite association of skarn W mineralization at Niutangjie district, South China Block. Ore Geol. Rev. 102, 268–283.

Chen, J., Wang, R.C., Zhu, J.C., Lu, J.J., Ma, D.S., 2013. Multiple-aged granitoids and related tungsten-tin mineralization in the Nanling Range, South China. Sci China Earth Sci. 56 (12), 2045–2055.

Chen, W., Zhang, W., Zhang, Y.Q., Jin, G.S., Wang, Q.L., 2006. Late Cenozoic episodic uplifting in southeastern part of the Tibetan plateau-evidence from Ar-Ar thermochronology. Acta Petrol. Sin. 22, 867–872 in Chinese with English abstract.

Crawford, M.L., 1981. Phase equilibria in aqueous fluid inclusions. In: Hollister, L.S., Crawford, M.L. (Eds.), Fluid Inclusions: Application to Petrology. Miner Assoc. of Canada Short Course Handbook. 6, 75-100.

Cuney, M., Barbey, P., 2014. Uranium, rare metals, and granulite-facies metamorphism. Geosci Front. 5 (5), 729–745.

Dai, Y.P., Yu, X.Q., Zhang, L.C., Cao, W.T., Zhu, Y.D., Li, C.L., 2014. Geology, isotopes and geochronology of the Caijiaping Pb-Zn deposit in the North Wuyi area, South China: implications for petrogenesis and metallogenesis. Ore Geol. Rev. 57, 116–131.

Darling, R.S., 1991. An extended equation to calculate NaCl contents from final clathrate melting temperatures in H_2O-CO_2-NaCl fluid inclusions: Implications for P-T, isochore location. Geochim. Cosmochim. Acta. 55 (12), 3869–3871.

Ding, X., Li, J.K., 2015. Ore-forming mechanism of the Asikaerte granitic pegmatite beryllium deposit in Xinjiang. China. Acta Geol Sin-Engl. 90, 1053–1054.

Dutrow, B.L., Henry, D.J., 2011. Tourmaline: a geologic DVD. Elements. 7 (5), 301–306.

Dyar, M.D., Wiedenbeck, M., Robertson, D., Cross, L.R., Delaney, J.S., Ferguson, K., Francis, C.A., Grew, E.S., Guidotti, C.V., Hervig, R.L., Hughes, J.M., Husler, J., Leeman, W., McGuire, A.V., Rhede, D., Rothe, H., Paul, R.L., Richards, I., Yates, M., 2001. Reference minerals for the microanalysis of light elements. Geostand. Newslett. 25, 441–463.

Fei, G., Menuge, J.F., Chen, C., Yang, Y., Deng, Y., Li, Y., Zheng, L., 2021. Evolution of pegmatite ore-forming fluid: the Lijiagou spodumene pegmatites in the Songpan-Ganzi Fold Belt, southwestern Sichuan Province, China. Ore Geol. Rev. 139, 104441.

Giuliani, G., France-Lanord, C., Zimmermann, J.L., Cheilletz, A., Arboleda, C., Charoy, B., Coget, P., Fontan, F., Giard, D., 1997. Fluid composition, δD of channel H_2O, and $\delta^{18}O$ of lattice oxygen in beryls: genetic implications for Brazilian, Colombian, and Afghanistan emerald deposits. Int. Geol. Rev. 39, 400–424.

Goldstein, R.H., Reynolds, T.J., 1994. Systematics of fluid inclusions in diagenetic minerals: SEPM Short Course. 31, 199.

Harangi, S.Z., Downes, H., Kósa, L., Szabó, C.S., Thirlwall, M.F., Mason, P.R.D., Mattey, D., 2001. Almandine garnet in calc-alkaline volcanic rocks of the Northern Pannonian Basin (Eastern-Central Europe): geochemistry, petrogenesis and geodynamic implications. J. Petrol. 42 (10), 1813–1843.

He, S.W., Wang, K.X., Liu, X.D., Lei, Y.L., 2022. Genesis of the Yihuang strong peraluminous S-type granite in Jiangxi Province and its constraints on Early Paleozoic intracontinental orogeny in South China. Geol. Bull. China 41, 788–909.

Henry, D.J., Guidotti, C.V., 1985. Tourmaline as a petrogenetic indicator mineral-an example from the staurolite-grade metapelites of NW Maine. Am. Mineral. 70, 1–15.

Henry, D.J., Novak, M., Hawthorne, F.C., Ertl, A., Dutrow, B.L., Uher, P., Pezzotta, F., 2011. Nomenclature of the tourmaline-supergroup minerals. Am. Mineral. 96 (5-6), 895–913.

Hu, Z.K., 2019. Study on the fluid inclusions and genesis of beryl in South Tibet. China University of Geosciences (Beijing). Master's thesis.

Hua, R.M., Zhang, W.L., Chen, P.R., Zhai, W., Li, G.L., 2013. Relationship between Caledonian granitoids and large-scale mineralization in South China. Geol. J. China Univ. 19, 1–11 in Chinese with English abstract.

Huang, W.Q., Shui, T., Ni, P., 2017. Study on fluid inclusions of emeralds at Malipo deposit, Yunnan Province. Acta Mineral. Sin. 37, 75–83.

Hulsbosch, N., Hertogen, J., Dewaele, S., André, L., Muchez, P., 2014. Alkali metal and rare earth element evolution of rock-forming minerals from the gatumba area pegmatites (rwanda): quantitative assessment of crystal-melt fractionation in the regional zonation of pegmatite groups. Geochim. Cosmochim. Acta. 132, 349–374.

Jiang, S.Y., Zhao, K., Jiang, H., Su, H., Xiong, S., Xiong, Y., Xu, Y., Zhang, W., Zhu, L., 2020. Spatiotemporal distribution, geological characteristics and metallogenic mechanism of tungsten and tin deposits in China: an overview. Chinese Sci. Bull. 65 (33), 3730–3745.

Jiang, S.Y., Wang, C.L., Zhang, L., Yuan, F., Su, H.M., Zhang, H.X., Liu, T., 2021. In situ trace element tracing and isotopic dating of pegmatite-type lithium deposits: an overview. Acta Geol. Sin. 95, 3071–13038.

Jingwen, M., Yanbo, C., Maohong, C., Pirajno, F., 2013. Major types and time-space distribution of Mesozoic ore deposits in South China and their geodynamic settings. Miner. Deposita. 48 (3), 267–294.

Koppers, A.A.P., 2002. ArArCALC: software for $^{40}Ar/^{39}Ar$ age calculations. Comput. Geosci. 28 (5), 605–619.

Li, J., Huang, X.L., He, P.L., Li, W.X., Yu, Y., Chen, L.L., 2015. In situ analyses of micas in the Yashan granite, South China: constraints on magmatic and hydrothermal evolutions of W and Ta-Nb bearing granites. Ore Geol. Rev. 65, 793–810.

Li, J., Huang, X.L., Fu, Q., Li, W.X., 2021. Tungsten mineralization during the evolution of a magmatic-hydrothermal system: mineralogical evidence from the Xihuashan rare-metal granite in South China. Am Mineral. 106, 443–460.

Li, W.J., Liang, J.C., Feng, Z.H., Zhang, G.L., Chen, M.H., Yuan, A.P., 2006. Judging for characteristics of geochemical and structural environment of several Caledonian granitoids in northeast Guangxi: Min. Resour. Geol. 20, 353–360 in Chinese with English abstract.

Li, J.K., Liu, X.F., Wang, D.H., 2014. The metallogenic regularity of lithium deposit in China. Acta Geol. Sin. 88, 2269–2283 in Chinese with English abstract.

Li, L.-M., Sun, M., Wang, Y., Xing, G., Zhao, G., Lin, S., Xia, X., Chan, L., Zhang, F., Wong, J., 2011a. U-Pb and Hf isotopic study of zircons from migmatised amphibolites in the Cathaysia Block: implications for the early Paleozoic peak tectonothermal event in Southeastern China. Gondwana Res. 19 (1), 191–201.

Li, X.F., Yu, Y., Wang, C.Z., 2011b. Caledonian granitoids in the Jinxiu area, Guangxi, South China: implications for their tectonic setting. Lithos 272–273, 249–260.

Li, J.K., Zou, T.R., Wang, D.H., Ding, X., 2017. The metallogenic regularity of beryllium deposits in China. Mineral Deposits 36, 951–978.

Linnen, R.L., Van Lichtervelde, M., Cerny, P., 2012. Granitic pegmatites as sources of strategic metals. Elements 8 (4), 275–280.

Liu, Z.S., 1975. Beryllium geochemical characteristics of granitoids from different ages in South China. Geochimica 01, 42–54.

Liu, Y., Gao, S., Hu, Z., Gao, C., Zong, K., Wang, D., 2010. Continental and oceanic crust recycling-induced melt-peridotite interactions in the trans-North China Orogen: U-Pb dating, Hf isotopes and trace elements in zircons from mantle xenoliths. J. Petrol. 51 (1-2), 537–571.

Liu, Y., Deng, J., Shi, G.H., Sun, X., Yang, L.Q., 2012. Genesis of the Xuebaoding W-Sn-Be crystal deposits in Southwest China: evidence from fluid inclusions, stable isotopes and ore elements. Resour. Geol. 2, 159–173.

Liu, S., Wang, R., Jeon, H., Hou, Z., Xue, Q., Zhou, L., Chen, S., Zhang, Z., Xi, B., 2020. Indosinian magmatism and rare metal mineralization in East Tianshan orogenic belt: an example study of Jingerquan Li-Be-Nb-Ta pegmatite deposit. Ore Geol. Rev. 116, 103265.

Liu, X., Wang, Q., Ma, L., Yang, J.-H., Ma, Y.-M., Huang, T.-Y., 2021. Early Paleozoic and Late Mesozoic crustal reworking of the South China Block: Insights from Early Silurian biotite granodiorites and Late Jurassic biotite granites in the Guangzhou area of the south-east Wuyi-Yunkai orogeny. J Asian Earth Sci. 219, 104890.

London, D., 1986. Magmatic-hydrothermal transition in the Tanco rare-elements pegmatite: evidence from fluid inclusions and phase equilibrium experiments. Am. Mineral. 71, 376–395.

London, D., 2005. Granitic pegmatites: an assessment of current concepts and directions for the future. Lithos 80 (1-4), 281–303.
Long, Z.Y., Yu, X.Y., Jiang, X., Guo, B.J., Ma, C.Y., You, Y., Zheng, Y.Y., 2021. Fluid boiling and fluid-rock interaction as primary triggers for emerald deposition: Insights from the Dayakou emerald deposit (China). Ore Geol. Rev. 139, 104454.
Luo, X., Xia, Q.X., Zheng, Y.F., Li, W.C., 2022. An experimental study of partial melting of metafelsic rocks: constraints on the feature of anatectic melts and the origin of garnets in collisional orogens. J. Earth Sci 33 (3), 753–769.
Lv, Z.H., Zhang, H., Tang, Y., Liu, Y.L., Zhang, X., 2018. Petrogenesis of syn-orogenic rare metal pegmatites in the Chinese Altai: evidences from geology, mineralogy, zircon U-Pb age and Hf isotope. Ore Geol. Rev. 95, 161–181.
Lv, Z.H., Zhang, H., Tang, Y., 2021. Anatexis origin of rare metal/earth pegmatites: Evidences from the Permian pegmatites in the Chinese Altai. Lithos 380-381, 105865.
Mao, J.W., OuYang, H.G., Song, S.W., Santosh, M., Yuan, S.D., Zhou, Z.H., Zheng, W., Liu, H., Liu, P., Cheng, Y.B., Chen, M.H., 2019. Geology and metallogeny of tungsten and tin deposits in China. SEG 22, 411–482.
Marschall, H.R., Jiang, S.Y., 2011. Tourmaline isotopes: no element left behind. Elements 7 (5), 313–319.
Martin, R.F., De Vito, C., 2005. The patterns of enrichment in felsic pegmatites ultimately depend on tectonic setting. Can. Mineral. 43 (6), 2027–2048.
McDonough, W.F., Sun, S.S., 1995. The composition of the Earth. Chem Geol. 120 (3–4), 223–253.
Michallik, R.M., Wagner, T., Fusswinkel, T., Heinonen, J.S., Heikkilä, P., 2017. Chemical evolution and origin of the Luumäki gem beryl pegmatite: constraints from mineral trace element chemistry and fractionation modeling. Lithos 274–275, 147–168.
Morgan, G.B., London, D., 1989. Experimental reactions of amphibolite with boron-bearing aqueous fluids at 200 MPa: implications for tourmaline stability and partial melting in mafic rocks. Contrib. Mineral. Petrol. 102 (3), 281–297.
Mulja, T., Williams-Jones, A.E., 2018. The physical and chemical evolution of fluids in rare-element granitic pegmatites associated with the Lacorne pluton, Québec. Canada. Chem Geol. 493, 281–297.
Müller, A., Kearsley, A., Spratt, J., Seltmann, R., 2012. Petrogenetic implications of magmatic garnet in granitic pegmatites from southern Norway. Can. Mineral. 50 (4), 1095–1115.
Müller, A., Romer, R.L., Pedersen, R.B., 2017. The Sveconorwegian Pegmatite Province - thousands of pegmatites without parental granite. Can. Mineral. 55, 1–33.
Palmer, M.R., Slack, J.F., 1989. Boron isotopic composition of tourmaline from massive sulfide deposits and tourmalinites. Contrib. Mineral. Petrol. 103 (4), 434–451.
Partington, G.A., Mcnaughton, N.J., Williams, I.S., 1995. A review of the geology, mineralization, and geochronology of the Greenbushes pegmatite, western Australia. Econ. Geol. 90, 616–635.
Pauly, C., Gysi, A.P., Pfaff, K., Merkel, I., 2021. Beryl as indicator of metasomatic processes in the California Blue Mine topaz-beryl pegmatite and associated miarolitic pockets. Lithos 404-405, 106485.
Qin, J.L., 2014. Geological characteristics of the Shayikenbulake pegmatite beryllium ore deposit in Altai, Xinjiang. Xinjiang University. Master's thesis.
Raimbault, L., Cuney, M., Azencott, C., Duthou, J.L., Joron, J.L., 1995. Geochemical evidence for a multistage magmatic genesis of Ta-Sn-Li mineralization in the granite at Beauvoir, French Massif Central. Econ. Geol. 90, 548–576.
Romer, R.L., Heinrich, W., Schröder-Smeibidl, B., Meixner, A., Fischer, C.-O., Schulz, C., 2005. Elemental dispersion and stable isotope fractionation during reactive fluid-flow and fluid immiscibility in the Bufadel Diente aureole, NE-Mexico: evidence from radiographies and Li, B, Sr, Nd, and Pb isotope systematics. Contrib. Mineral. Petrol. 149 (4), 400–429.
Selway, J.B., Breaks, F.W., Tindle, A.G., 2005. A review of rare-element (Li-Cs-Ta) pegmatite exploration techniques for the Superior Province, Canada, and large worldwide tantalum deposits. Explor. Min. Geol. 14, 1–30.
Shu, L., Wang, B., Cawood, P.A., Santosh, M., Xu, Z.Q, 2015. Early Paleozoic and Early Mesozoic intraplate tectonic and magmatic events in the Cathaysia Block, South China. Tectonics 34 (8), 1600–1621.
Shu, L.S., Yu, J.H., Jia, D., Wang, B., Shen, W.Z., Zhang, Y.Q., 2008. Early Paleozoic orogenic belt in the eastern segment of South China. Geol. Bull. China 27, 1581–1593.
Song, M.J., Shu, L.S., Santosh, M., Li, J.Y., 2015. Late Early Paleozoic and Early Mesozoic intracontinental orogeny in the South China Craton: geochronological and geochemical evidence. Lithos 232, 360–374.
Steiger, R.H., Jäger, E., 1977. Subcommission on geochronology: convention on the use of decay constants in geo- and cosmochronology. Earth Planet. Sci. Lett. 36 (3), 359–362.
Tang, Y., Zhao, J.Y., Zhang, H., Cai, D.W., Lv, Z.H., Liu, Y.L., Zhang, X., 2017. Precise columbite-(Fe) and zircon U-Pb dating of the Nanping No. 31 pegmatite vein in northeastern Cathaysia Block. SE China. Ore Geol. Rev. 83, 300–311.
Tian, E., Wang, R.C., Xie, L., Zhang, W.L., Che, X.D., Zhang, R.Q., 2020. Mineralogy and geochemistry of the discovered Late Mesozoic granite-pegmatite and associated Sn-Nb-Ta-Be mineralization in the Miao'ershan-Yuechengling composite batholith, northern Guangxi. South China. J Asian Earth Sci. 41, 104149.
Tonarini, S., Pennisi, M., Adorni-Braccesi, A., Dini, A., Ferrara, G., Gonfiantini, R., Wiedenbeck, M., Gröning, M., 2003. Intercomparison of boron isotope and concentration measurements. Part I: selection, preparation and homogeneity tests of the intercomparison materials. Geostand. Geoanal. Res. 27, 21–39.
Trumbull, R.B., Beurlen, H., Wiedenbeck, M., Soares, D.R., 2013. The diversity of B-isotope variations in tourmaline from rare-element pegmatites in the Borborema Province of Brazil. Chem. Geol. 352, 47–62.
Wang, S.S., 1983. Age determinations of ^{40}Ar-^{40}K, ^{40}Ar-^{39}Ar and radiogenic ^{40}Ar released characteristics on K-Ar geostandards of China. Sci. Geol. Sin. 4, 315–323.
Wang, Y.J., Fan, W.M., Sun, M., Liang, X.Q., Zhang, Y.H., Peng, T.P., 2007a. Geochronological, geochemical and geothermal constraints on petrogenesis of the Indosinian peraluminous granites in the South China Block: a case study in the Hunan Province. Lithos 96 (3-4), 475–502.
Wang, Y.J., Fan, W.M., Zhao, G.C., Ji, S.C., Peng, T.P., 2007b. Zircon U-Pb geochronology of gneissic rocks in the Yunkai massif and its implications on the Caledonian event in the South China Block. Gondwana Res. 12 (4), 404–416.
Wang, Y.J., Zhang, A.M., Fan, W.M., Zhao, G.C., Zhang, G.W., Zhang, Y.Z., Zhang, F.F., Li, S.Z., 2011. Kwangsian crustal anatexis within the eastern South China Block: Geochemical, zircon U-Pb geochronological and Hf isotopic fingerprints from the gneissoid granites of Wugong and Wuyi-Yunkai Domains. Lithos 127 (1–2), 239–260.
Wen, C.H., Shao, Y.J., Xiong, Y.Q., Li, J.K., Jiang, S.Y., 2021. Ore genesis of the Baishawo Be-Li-Nb-Ta deposit in the northeast Hunan Province, south China: evidence from geological, geochemical, and U-Pb and Re-Os geochronologic data. Ore Geol. Rev. 129, 103895.
Wolf, M., Romer, R.L., Franz, L., López-Moro, F.J., 2018. Tin in granitic melts: the role of melting temperature and protolith composition. Lithos 310–311, 20–30.
Xiong, F., Tao, Y., Deng, X.Z., 2015. Characteristics of fluid inclusion and genesis of Mahuaping tungsten-beryllium deposit, Yunnan. Acta Mineral Sin. 35, 353–354.
Yan, Q.H., Wang, H., Chi, G., Wang, Q., Hu, H., Zhou, K., Zhang, X.Y., 2022. Recognition of a 600-km-long late Triassic rare metal (Li-Rb-Be-Nb-Ta) pegmatite belt in the western Kunlun Orogenic belt, western China. Econ. Geol. 117, 213–236.
Yang, Q., Chen, B., Zhao, H., 2020. Fluid evolution of Li-rich pegmatite- a case study of Jiajika and Dahongliutan Li-rich pegmatite deposits in western Sichuan. Annual Meeting of China Earth Science Association. 231–232.
Yin, R., Han, L., Huang, X.L., Li, J., Li, W.X., Chen, L.L., 2019. Textural and chemical variations of micas as indicators for tungsten mineralization: evidence from highly evolved granites in the Dahutang tungsten deposit. Am. Mineral. 104, 949–965.
Yuan, S.D., Williams-Jones, A.E., Romer, R.L., Zhao, P., Mao, J.W., 2019. Protolith-related thermal controls on the decoupling of Sn and W in Sn-W metallogenic provinces: insights from the Nanling region, China. Econ. Geol. 114, 1005–1012.
Zeng, Q., Liu, J., Qin, K., Fan, H., Chu, S., Wang, Y., Zhou, L., 2013. Types, characteristics, and time-space distribution of molybdenum deposits in China. Int Geol. Rev. 55 (11), 1311–1358.
Zhang, F.R., Shu, L.S., Wang, D.Z., Yu, J.H., Shen, W.Z., 2009. Discussion on the tectonic setting of Caledonian granitoids in the eastern segment of South China. Front Earth Sci. 16, 248–260.
Zhao, H., Jiang, S., Dai, B., Ma, L., Li, J., 2015. Geochronology and Hf isotope study of pegmatite in the Xiaoqinling area of NW China: implication for petrogenesis and regional metamorphism. J. Earth Sci. 26 (3), 295–305.
Zhao, X., Li, L., Xu, M., Liu, H., Zhu, Q., Jin, G., Jiang, Y., 2021. Control of basement on Paleozoic mineralizations in the Wuyi metallogenic belt. Ore Geol. Rev. 131, 104037.
Zheng, W., Mao, J.W., Liao, Z.Q., Luo, P., Hua, Z.H., Du, G.X., Chen, W., Zheng, Z.C., Huang, H.X., Ren, Z.N., Chu, K.L., Wu, S.H., Yu, K.K., Song, S.W., 2023. Discovery and prospecting potentiality of the Caledonian supergiant pegmatite deposit in the Weiling, Jiangxi Province. Geology in China. 1–3.
Zhong, J., Chen, Y.J., Pirajno, F., 2017. Geology, geochemistry and tectonic settings of the molybdenum deposits in South China: a review. Ore Geol. Rev. 81, 829–855.
Zou, T.R., Li, Q.C., 2006. Rare and rare earth metallic deposits in Xinjiang, China. Geological Publishing House, Beijing 1–284 in Chinese with English abstract.